Article:
Bouhlel, S, Leach, DL, Johnson, CA et al. (3 more authors) (2016) A salt diapir-related Mississippi Valley-type deposit: the Bou Jaber Pb-Zn-Ba-F deposit, Tunisia: fluid inclusion and isotope study. Mineralium Deposita, 51 (6). pp. 749-780. ISSN 0026-4598

https://doi.org/10.1007/s0126-015-0634-8

Geologic, mineralogic, fluid inclusion and isotope evidence for the genesis of the Bou Jaber Ba-F-Pb-Zn salt diapir-related Mississippi Valley-Type deposit, Tunisia

Salah Bouhlel, David L. Leach, Craig A. Johnson, Sihem Salmi-Laouar, Erin Marsh, David A. Banks

Salah Bouhlel

University Tunis el Manar, Faculty of Sciences of Tunis Tunisia

D. L. Leach.

Colorado School of Mines, Department of Geology and Geological Engineering, Golden, Colorado 80401 U.S.A.

C. A. Johnson, E.E. Marsh

U.S. Geological Survey, Box 25046 Federal Center, Denver, Colorado, 80225, U.S.A.

S. Salmi-Laouar

University Badji Mokhtar Annaba, Algeria

D. Bank

School of Earth and Environment, University of Leeds, Woodhouse Lane, Leeds, LS2 9JT, U.K.

Abstract The Bou Jaber Ba-F-Pb-Zn deposit is located at the edge of a Triassic salt diapir in the Salt Diapir Belt of the Tunisian Atlas Foreland. It provides a good example of the close association between Mississippi Valley-type mineralization and evaporite-bearing diapirs.The ores are fault-controlled and occur as subvertical column-shaped bodies developed in dissolution breccias and cavities in Aptian platform/reef limestone, which is covered unconformably by impermeable shale and marl of the Upper Albian-Cenomanian. The limestone host rock is hydrothermally altered to ankerite proximal to and within the ore bodies. Quartz as fine-grained bipyramidal crystal formed during hydrothermal alteration of the host rocks. The ore mineral assemblage is composed of barite, fluorite, sphalerite and galena in decreasing abundance. The ore zones outline distinct depositional events: sphalerite-galena, barite+ankerite and fluorite. Fluid inclusions, commonly oil-rich, have distinct fluids salinities and homogenization temperatures for each of these events: sphalerite-galena (17 to 24 wt% NaCl eq., and Th from 112° to 136°C; ankerite+ barite (11 to 17 wt% NaCl eq., and Th from 100° to 130°C); fluorite (19 to 21 wt% NaCl eq., Th from 140° to 165°C). The mean temperatures of the ore fluids in the events decreased from sphalerite (125°C) to barite (115°C) and increased during fluorite deposition (152°C); then decreased to ~110°C during late calcite precipitation. LA-ICP-MS analyses of fluid inclusions show there are at least 2 distinct fluids. Inclusions in fluorite are metal-rich (100's to 1000's ppm Pb, Zn, Cu, Fe) but the inclusions in barite are Pb, Zn, Cu, Fe-deficient. No information on metal contents are available. Inclusions in fluorite have Cl/Br and Na/Br ratios of several thousand, consistent with dissolution of halite while the inclusions analysed in barite have values lower than those of seawater which are indicative of a Br-enriched brine derived from the evaporation of seawater plus a component of halite dissolution. The salinity of the barite fluid inclusions is less than obtained simply by the evaporation of seawater to halite saturation and requires a dilution of more than two times for halite saturated fluids. This is consistent with the presence of a component of meteoric water in the brine that deposited barite. The higher K/Na values from fluid inclusions from barite suggest that the brines interacted with K-rich rocks in the basement or in siliciclastic sediments in the basin. Carbonate gangue minerals (ankerite and calcite) have $\delta^{13}C$ and $\delta^{18}O$ that are close to the Aptian limestone host rock values and indicate fluid equilibrium between carbonate host rocks and warm brines. The $\delta^{34}S$ values for sphalerite and galena are positive and very homogeneous. They fall within a narrow range (1 to 10 ‰) with a bulk value of 7.5 ‰, indicating a homogeneous source of sulfur. The $\delta^{34}S$ values of barite are also relatively homogeneous (22 ‰), with 6 ‰ higher than the $\delta^{34}S$ of local and regional Triassic evaporites (15‰). The latter are believed to be the source of sulfate. Temperature of deposition together with sulfur isotopes data indicate that the reduced sulfur in sulfides was derived through the reduction of Triassic sulfate by thermochemical sulfate reduction using hydrocarbons produced probably from Upper Cretaceous source rocks. The $^{87}Sr/^{86}Sr$ ratio in the Bou Jaber barite (0,709821 to 0.711408) together with the lead isotopes values of Bou Jaber galena ($^{206}Pb/^{204}Pb$=18.699 to 18.737; $^{207}Pb/^{204}Pb$=15.635 to 15.708 and $^{208}Pb/^{204}Pb$=38.321 to 38.947) show that

metals were extracted from homogenous crustal source(s). The tectonic setting of the Bou Jaber ore deposit, the carbonate nature of the host rocks, the epigenetic style of the mineralization and the mineral associations, together with sulfur and oxygen isotope data and fluid inclusion data show that Bou Jaber zinc-lead ores of the deposit has the major characteristics of a salt diapir-related MVT Zn-Pb ores with superimposed events of fluorite and of barite deposit. Field relations are consistent with mineral deposition during the Miocene Alpine Orogeny from multiple hydrothermal events: (1) Zn-Pb sulfides formed by the mixing of two fluids: one fluid metal-rich but reduced sulfur-poor and a second fluid reduced sulfur rich; (2) the fluorite precipitated from a more dilute fluid with higher temperatures; (3) barite precipitation involved the influx of a meteoric water component that mixed with a barium-rich fluid. A significant conclusion of the study provides evidence that decouples the mineral assemblages (Zn-Pb, fluorite and barite) into separate and possibly unrelated mineralization events. Consequently, the presence of barite or fluorite mineralization in any diapiric zone does not necessarily suggest the presence of Zn-Pb rich ores.

Keywords Fluid inclusions° Laser ablation ICP-MS° C, O, S, Sr, Pb isotopes° diapir-related MVT Ba-F-Pb-Zn deposits °Bou Jaber ° Tunisia°

Introduction

Lead-zinc ore deposits associated with evaporite-bearing diapirs are well known and have been exploited for many years in North Africa and the Gulf of Mexico region of the U.S.A. (Sainfeld 1956; Hanna and Wolf 1934; Price and Kyle 1983; Posey et al. 1994).They form a distinct group within the MVT class of deposits, with typically low to high tonnage and modest to high grade (1 to few million tons). Recently high tonnage (with a reserve of approximately 200 million tons of ore grading 6 % Zn and 1.3 % Pb are discovered in Jinding, China (e.g., Leach et al 2013). A number of North American studies have characterized some of the processes of formation (e.g., Light et al. 1987; Posey and Kyle 1988; Kyle and Price 1986; Kyle and Posey 1991).

In North Tunisia and adjacent Algeria region, although the numerous Pb-Zn (±Ba-F) deposits located at the edges of Triassic salt-bearing diapirs were exhaustively investigated and explored during the last eight decades, important aspects of the metallogeny of these salt diapir-related metallic deposits remain a subject of debate. Conflicting genetic models involving syngenetic origin, epigenetic origin, or a combination of both have been proposed (e.g., Sainfeld 1956; Rouvier et al. 1985; Gharbi et al. 1985; Charef and Sheppard 1987; Amouri 1989; Orgeval 1994; Sheppard et al. 1996; Bouzenoune and Lécolle 1997; Bouhlel 2005; Bouhlel et al 2007; Bouhlel et al. 2009).

The Bou Jaber evaporite diapir-related Ba-F-Pb-Zn deposit, is located in central-western Tunisia, 30 km west of Tajerouine city, and lies against the Algerian-Tunisian international border (Fig. 1). It is one of numerous Algerian-Tunisian Pb-Zn-Ba deposits located at the edges of Triassic diapirs and where mineralization is hosted in Cretaceous peridiapiric limestone strata (Sainfeld 1956; Rouvier et al. 1985; Bouhlel 1993). Unlike most of the Tunisian-Algerian salt diapir-related Pb-Zn deposits, the Bou Jaber deposit is barite and fluorite-rich and exhibits a clear spatial relationship with three geo-structural elements: a salt diapir and NW-trending faults limiting Miocene-Pliocene grabens, allowing a possible role of these three ore geological controls in its genesis.

Currently no comprehensive geochemical investigation has been published. Based on mapping, general mineralogical descriptions and limited geochemical database the controversy over the genesis of the Bou Jaber mineralization has mainly included: (i) a syngenetic origin that involved meteoric karstification followed by the deposition of base-metals originating from reworking of continental heavy-metal-rich soil horizons during Upper Aptian period (Fuchs 1973; Amouri 1989); and (ii) an epigenetic origin at Miocene time, that involved replacement of limestones and infilling of hydrothermal dissolution-cavities and open fractures by undefined fluids and precipitation processes (Bouhlel 1987; Bouhlel 1993; Salmi-Laouar et al. 2004).To better define ore controls, the mineralizing event (s); the nature, origin, and evolution of the hydrothermal fluids, metal and sulfur sources, and the processes that control metal precipitation, this study integrates the geologic ore controls, ore textures and paragenesis, fluid inclusions microthermometry,

halogen analyses of fluid inclusions, and stable (C, O) and radiogenic (Sr, Pb) isotope analyses from mineral separates. The results provide new insights into the origin of the Bou Jaber ore deposit and, in a more general sense, into the metallogenesis of the diapir-related carbonate-hosted Pb-Zn-Ba-F deposits.

Geological setting and regional mineralization

Bou Jaber deposit is located in the Salt Diapir Belt of the Tunisian Atlas foreland fold-thrust-belt which is a part of the Alpine Atlas mountain ranges extending through Morocco, Algeria and Tunisia, and resulting from the Miocene convergence between the Africa and Europe plates (Fig. 1).With its NE-SW-striking length of 200 km and a fairly constant width of 50 km, the Salt Diapir Belt roughly coincides with the Tunisian Trough (Fig. 1). It is bordered to the North by the Tell thrust belt characterized by Miocene south-directed tangential tectonism of Tellian and Numidian nappes and to the South by the Central Tunisia Platform. The south-western area of the Salt Diapir Belt and large area of the Central Tunisia Platform are intersected by large number of transverse grabens. The Tell thrust belt and the Tunisian Atlas foreland fold-thrust-belt are formed by about 8-10 km-thick Mesozoic-Tertiary folded cover pieced by a large number of Triassic salt diapirs. At the surface, the Triassic diapirs are mainly composed of chaotic breccias dominantly formed by gypsum with few shale, dolostone and basic volcanic that correspond to insoluble caprocks. The few wells drilled through diapirs encountered massive salt below 200 or 300 m of gypsum. In map view the diapirs occur as elongated SW-NE bodies, typically 10 x 3 km long and 1 to 2 km in width, and are distributed along 3 to 5 distinct parallel NE-SW– directed strike-slip faults that correspond to the reactivation of former Hercynian faults (Perthuisot 1978; Martinez and Truillet 1987; Turki et al. 1988; Chaari 2002).The Bou Jaber diapir is located on one of these diapir-bearing faults (the Tajerouine Fault) (Fig. 1). Almost everywhere in the Salt Diapir Belt, the tectonic contacts between the Triassic salt diapirs and the intruded Cretaceous to Miocene rocks are marked by lens-shaped evaporite-dissolution breccia bodies that are the host of Pb-Zn-Sr mineralization (Rouvier et al. 1985; Sheppard 1996; Bouhlel 1993; Bouhlel et al. 2007).

The Triassic substratum is only known in the Saharan Platform by deep petroleum drilling. It is composed of Paleozoic shale, sandstone, arkosic sandstone and Precambrian granite or metamorphic rocks (Mejri et al. 2006). The Jurassic platform carbonate deposition of central and eastern Tunisia has only rarely been observed and is nowhere seen overlying the diapirs. Lower Cretaceous is composed of sandstone, clay and limestone. Upper Cretaceous - Eocene succession is composed of marl and argillaceous limestone. Oligocene and Miocene are discordant and composed of continental clay, sandstone and conglomerate. This Mesozoic-Tertiary succession forms SW-NE-trending folds (acquired since the Oligocene) which are cut by NW-SE-directed faults, limiting grabens filled by Mio-Pliocene continental sediments.

During the Triassic to Lower Tertiary (pre-orogenic period), the instability of the sedimentary basement was almost permanent, related to repeated activity of deep accidents, inherited from Panafrican and Hercynian orogens and reactivated mainly during rifting stages related to the Africa-Europe drift movement (Cohen et al. 1980; Guirand and Maurin (1991). These resulted in a N-S extension that persisted from the Jurassic until Lower Aptian. In this context, the north-central Tunisia corresponded to a rifted continental margin characterized by extensional NE-SW and NW-SE-trending faults limiting horsts, grabens and tilted

blocks (Boltenhagen 1985; Martinez and Truillet 1987), with particularly the individualization since the Neocomian of two differentiated paleogeographic and sedimentary domains (Figs, 1-2): to the north, a deep rifted basin called the Tunisian Trough (Burollet 1956) and to the south the flat Central Tunisia Platform which is the northern extension of the Saharan Platform (Vially et al. 1994). In the Tunisian Trough, the syn-rift sedimentary sequence is very thick (about 5,000 m in the Cretaceous alone in the El Kef area) and is composed of deep marine sediments mainly marl and argillaceous limestone. On the platform area, the thicknesses are reduced and gaps occur locally in the series; the facies are composed of sandstone and clay with shallow marine limestone and dolostone of Aptian age (Marie et al. 1084; M'Rabet 1987).

In the trough, with the overburden of Jurassic and Neocomian series, halokinetic movements of the Triassic salt began. In several places of the south-western area of the trough (Tajerouine-Tabessa region), about 300 to 500 m-thick Aptian, and Lower Albian shallow marine bioclastic limestones, including reef development, overlay diapiric structures (e.g., Bou Jaber, Slata, and Ouenza; Perthuisot 1978, Bouhlel 1987). Aptian and Lower Albian limestones, on both Central Tunisia Platform and diapiric structures, are the host of siderite or Pb-Zn-Ba-F mineralization.

Transpression and transtension tectonics occurred during the Middle Albian with the reactivation of syn-rift extensional NE-SW and NW-SE-trending faults, limiting tilted blocks and half-grabens. It were the intersection zones of these fault systems that accelerated salt diapirism and where numerous diapirs intruded their roof and emerged onto the seafloor (Bolze 1954;Perthuisot 1981). Salt diapirs, tilted blocks, and half-grabens will control the distribution and the nature of the sedimentary facies (Boltenhagen 1985; Perthuisot 1981).

During the Upper Albian-Lower Turonian, transgressive post-rift shale and marl pelagic sediments (300 to 1000m-thick) invaded the entire Aptian-Lower Albian platform as well as the Tunisian Trough fossilizing uplifted blocks, half-grabens and salt diapirs. The latter structures, together with the upper Albian unconformity controlled the ore emplacements. The lower part of the transgressive series contains two organic-rich laminated black limestones: Upper Albian Mouelha laminites (~2 % COT) and Cenomanian-Turonian Bahloul laminites (up to 13% COT) (e.g., Saidi and Belayouni 1994; Soua 2009).These rocks are considered as excellent hydrocarbon source rocks for the petroleum system in the region (e.g., Saidi and Belayouni 1994; Soua 2009). Bahloul laminites may also be the host of strata-bound replacement-type sphalerite-rich mineralization as the case in Bou Grine (Bouhlel et al. 2009). The Cretaceous sedimentation continues with the deposition of about 2000 m-thick marl and limestone succession of Middle Turonian to Paleocene. Subsidence and transpressional tectonics caused a second diapiric piercement during the Lower Eocene (Perthuisot 1981).

The tectonic period of the Alpine orogeny in northern Tunisia began in Oligocene time and reached its maximum during the Middle Miocene time as a result of collision of microplates rifted off the European margin with the North African margin, and coincided with the progressive elimination of Proto-

Mediterranean lithosphere from west to east along the African margin (Rouvier 1977; Martinez and Truillet 1987). Deformations consist of a NW-SE contraction phase with significant shortening resulting in NE-SW to E-W-trending folds; flow of Triassic salt into the cores of these folds assisted by tectonic loading during fault inversion; NE-SW strike-slip faults resulting from reactivation of syn-rift extensional faults; and setting up in the North of the Tell Thrust Belt composed of major thrust sheets of Oligo-Lower Miocene "Numidian" flysch emplaced over Upper Cretaceous-Eocene "Tellian" nappes. At the base of the nappes, blades of Triassic evaporitic breccias are common; these are due to detachment surfaces or to diapiric extrusions cut and trailed by moving nappes. Basic and acidic igneous rocks are described in several places of the Tell Thrust Belt (e.g. Oued Bélif region and at La Galite island (Bellon 1976; Lardhi-Ouazza 1994) and correspond to Upper Miocene and Pliocene magmatism activities. In the Atlas Foreland, Pliocene reactivation of transpressional movements created NW-SE-trending grabens (Ben Ayed 1986; Chihi 1995) intersecting and cutting across the SW-NE-oriented folds and Triassic diapirs. The grabens were filled by Pliocene continental conglomerate and sandstone sediments. On the Tell Thrust Belt post-orogenic relaxation phase resulted in conglomerate, clay and lacustrine limestone deposition in Upper Miocene basins. Upper Miocene-Pliocene basins in the Atlas Foreland and in the Tell Thrust Belt are the host of some Pb-Zn ore deposits.

Ore deposits

The Pb-Zn ±(Ba, Sr, F) ore deposits in the Salt Diapir Belt and adjacent regions are shown on Figure1. Most of the ore deposits contain low to medium size resources (1 to 8 million tons at about 5 to 15 % Pb+Zn). The ore deposits are classified into four groups based on the ore minerals present in the deposits (Rouvier et al. 1985; Bouhlel 1993; Bouhlel 2005) (Fig. 1). However, we point out in this report that these groups are spatially and genetically distinct from each other. These assemblages are not present in all deposits and where they do occur, they may or may not be present in specific mineralized zones. In all cases, where they occur in the same mineralized zone, there is a consistent paragenetic relationship discussed later. These 4 groups reflect a complex hydrothermal overprinting by up to 4 mineralization events in some deposits. These ore groups are described below:

Group 1: Strata-bound replacement siderite deposits hosted in Aptian limestone (e.g., Ouenza, Bou Khadra and Jerissa deposits) with global resources of about 165 million tons of Fe metal (Pohl et al. 1986; Bouzenoune and Lecolle 1997).

Group 2: Ba±F±(Pb-Zn) strata-bound replacement-type and cavity-filling deposits in Aptian and Lower Albian platform and reef limestones at the edges of Triassic salt diapirs. This group shows two distinct mineral assemblages: group 2a with Ba-F±(Pb-Zn) (e.g., Mesloula, Mzouzia, Belkfif deposits in Algeria; Akrour et al. 1991; and Bou Jaber in Tunisia), and group 2b with Ba±(Pb-Zn) deposits (e.g., Slata, Hamra, Ajred, Trozza, in Tunisia) (Bouhlel 1993; Jrad and Perthuisot 1995; Béjaoui et al. 2013). Furthermore Pb-Zn-Ba mineralization is also present in the Cenomanian-Turonian dolostones (Aïn Nouba), in the Eocene

phosphorite rocks (Sekarna) and even in the Mio-Pliocene clastic rocks (Aïn Khmouda) (Sainfeld 1956; Fucks 1973; Garnit et al. 2012).

Group 3: Pb-Zn (±celestite) strata-bound replacement-type deposits hosted by dissolution evaporitic breccias at the contact zones between salt diapirs or salt sheets and the surrounding Cretaceous to Miocene rocks (e.g., Fedj el Adoum, Kebbouch, Bou Khil, Garn Halfaya, Zag Ettir, Aguiba). The most economic is the Fedj el Adoum deposit that contains about 1.5 Mt of 17% Zn+Pb (Sheppard et al. 1996; Bouhlel et al. 2007). If the barite is present in these deposits, it always cuts the celestite-, and the Pb-Zn ore bodies.

Group 4: Pb-Zn strata-bound replacement-type and vein-type ore deposits that lack Ba, Sr or F are hosted by Upper Cretaceous limestone that envelops the Triassic salt diapirs (Bou Grine, Akhouat, O. Jebs; Schmith 1999; Bouhlel et al. 2009; Béjaoui et al. 2013). Prior to mining operations (1992-2006), the Bou Grine deposit resources were about 7.3 million tons of ore at 15% Zn+Pb (Orgeval 1994).

Group 5: Pb-Zn deposits occur either as strata-bound ores or as veins in continental Mio-Pliocene strata (e.g., Sidi Driss in the Tell Thrust Belt and Koudiat Safra and Jebba in the Atlas Foreland) (Rouvier et al. 1985; Decrée et al. 2008).

Field observations indicate that the Zn-Pb-, Ba-F ores may be arranged as follow: a Zn-Pb event, a BaSO4 event (may have trace sphalerite and galena) and a fluorite event with minor barite (may have trace sphalerite and galena). These various mineral assemblages are suggestive of contributions from at least 4 distinct ore fluids and/or ore forming events that variably affected the Triassic diapiric structures. The Bou Jaber deposit contains a mineral assemblage that reflects mineralization from a Zn-Pb event, a barite event and a late fluorite event as discussed below.

The Bou Jaber deposit

The Bou Jaber deposit was first mined for lead and silver by the Romans (2^{th} to 5^{th} centuries), where galena yielded up to 500g/t Ag. Small and episodic mining activities continued by Arabs and Turks (9^{th} to 17^{th} centuries), and then the French (1890 to 1950). The most recent (1972 to 2004) intermittent mining activitiesby Tunisian state-owning mining companies focused on underground exploitation with a total production of about 50,000t Pb+Zn, 0.5 Mt barite and minor quantities of fluorite. The production ceased in late 2004 due to difficulties in the economic viability of the mine. The remaining estimated reserves are located mainly at the “Gîte de l’Est” (the east deposit), and are of about 8 Mt with a grade of 1.5% Pb, 3.5% Zn, 33 % $BaSO_4$, and 9% CaF_2. In 2015, European Industrial and base metal Limited concluded negotiations with the Tunisian Government and earned a 90% right in the Bou Jaber mine exploitation, while 10% are detained by the Office National des Mines (O.N.M.).

Lithostratigraphy and structural evolution

The geological map, lithostratigraphy and cross sections at Bou Jaber region are presented on Figure 3. The dipiric Triassic salt formation outcrops in the core of a Cretaceous anticline and consists of dissolution-mega breccias composed of chaotic assemblage of gypsum masses containing blocks of variegated argillite. Halite rocks are dissolved at the surface. These gypsum-rich breccias, partly covered by Mio-Pliocene continental sediments and alluvium, are similar of other Triassic outcrops in neighbouring diapirs where deep drill holes showed thick halite-rich zone beneath the gypsum breccia zone.

The Aptian-Lower Albian limestone (Serdj Formation) outcrops at the south flank of the diapir. It is composed of two platform and reef limestone members, respectively Aptian and Lower Albian in age (Dubourdieu 1956, Bouhlel 1993; Vila and Charrière 1993; Braham et al 2002). The Aptian limestone member is composed of 200 m-thick bioclastic limestone thickening up, interbedded by marl sequences (units 1-4,), following is a massive lens-shaped bar 50 to 100 m-thick (unit 5) composed of platform limestone containing rudistid and coral reefs. Following is a marl-rich member of about 100 m-thick (unit 6) consisting essentially of alternating marl, shale, fine-grained sandstone and bioclastic limestone. The Lower Albian limestone member (unit 7) forms a lens-shaped bar (250 to 50 m-thick) composed of metric-thick beds of bioclastic limestone containing abundant debris of Rudistids, Corals and Echinoderms.

In the southern flank of Bou Jaber Mountain, the shales and marls of the Upper Albian overlain from east to west the units 4 to 7 of the Aptian-Lower Albian platform succession (Fig. 3a). This spectacular cartographic discordance corresponds to the Aptian/Upper Albian unconformity (Bouhlel 1993), regionally known as the Austrian unconformity (Mejri et al 2006 and references therein). The Upper Albian-Cenomanian sequence begins with a small “block complex” (1 to 5 m-thick) composed of limestone blocks of 0.5 to 3 m across ripped from the nearby Aptian uplifted blocks, and in turn covered by about 600m-thick shale, finely laminated dark biomicrite limestone and marl (Fahdene Formation including the Mouelha-, and the Bahloul organic-rich laminite members). To the south (outside Fig. 3a), the Upper Cretaceous series continue with marine sediments of the Turonian to Eocene ages, consisting essentially of alternating marl and argillaceous limestone (1000 m-thick). The stratigraphic section continues with the Oligocene-Miocene series. The Oligocene-Early Miocene times is represented by sandstones and clays. The Late Miocene consists of continental molasses, sandstones and clays, 2,000 m thick, discordant on a regional scale, on earlier folded series.

From a structural point of view, The Bou Jaber E-W- to SE-NE-trending diapiric structure corresponds to a complex southeast-overturned anticline formed by Cretaceous marine strata that are pierced by a Triassic salt diapir. This structural organization is the result of a long-live salt diapir halokinesis and piercement that begun during the Aptian and continued during the compression, faulting and thrusting events of the Miocene Alpine orogeny. During these events, the Aptian/Upper Albian unconformity is overprinted

by the E-W to NE-SW-trending Bou Jaber Fault (Bouhlel 1987). Furthermore numerous N-S to NW-SE trending faults cut the peridiapiric Cretaceous strata into a number of displaced blocks and the NE termination of the Bou Jaber diapiric structure is intersected by the NW-trending Bou Ghanem graben filled by Miocene and Pliocene continental conglomerate, sandstone and clay.

Mineralization

The known carbonate-hosted mineralization at Bou Jaber diapiric structure forms several small to medium size deposits, fault-controlled and hosted by peridiapiric strata of the Aptian and Lower Albian platform limestone. The deposits are dominated by barite or sphalerite+galena or fluorite: Pb+Zn+Ba at the "gîte du col"; Pb-calcite at the "gîte du centre" ; Pb-Zn+calcite at the "gîte Esperance"; and Ba-F±Pb-Zn at the "gîte de l'Est" (Fig. 3a). This indicates that the western deposits are dominated by Pb-Zn and the eastern deposits are dominated by Ba-F (with minor Pb and Zn). Fluorite-rich zones are probably genetically related to the NW-trending faults limiting the Bou Ghanem graben.

The "gîte de l'Est" mineralization (Fig. 4) is hosted in the unit 5 of the Aptian platform/reef limestone which is uncomfortably overlain by mid-upper Albian-Cenomanian shale and marl. Mineralization fills breccia bodies and hydrothermal dissolution cavities distributed along roughly E-W faulted zones overprinting the Aptian/Upper Albian unconformity. Ore rich zones are often located at the intersection zones of NE- and NW-trending faults. In the central part of the deposit, near shaft 5, rich ores form three roughly vertical ore bodies termed A, B and C (Fig. 4d). Each of these ore bodies has a thickness of 5 to 40 m, and is roughly E-W-striking length of about 500 to 700m and extends to a depths greater than 400 m. Underground mapping and drill holes show that most ore bodies have the following zonation, from the border to the ore body core: sulfide rich-zone, mixed barite/sulfide zone and late barite rich-zone.

A number of liquid hydrocarbon seeps occur along fractures and within various porous zones of the permeable Aptian host limestone and as impregnations and residue within the ores. It consists of degraded liquid hydrocarbons composed of saturated hydrocarbon (18.9%), aromatic (7.2%), asphaltene (55.6%), and resin (18.3%) (Maameri and Daadouch 1986). The total of the heavy hydrocarbon fraction is about 74%, and the resin/asphaltene ratio is 0.34% (Maameri and Daadouch 1986). Potential source rocks belong to the Upper Albian-Cenomanian calcareous shales of the Fahdene Formation, containing ~2 wt% to ~13 wt% COT (Saidi and Belayouni 1994). This organic-rich formation was buried during the Campanian-Eocene period to a depth of about 3,000 m and organic maturation processes produced oil and gas as demonstrated by the numerous oil seeps in the Bou Jaber mine and neighbouring regions and by oil wells sourced from the Aptian limestone in the Central Tunisian Platform (e.g., Douleb and Semmama oil fields; Belayouni et al. 1992). Oil generation probably began in the Maastrichtian-Eocene times, resulting from subsidence, but peak petroleum generation probably occurred in the Miocene and Pliocene (Belayouni et al. 1992) in parallel with the Alpine orogenic events.

In the absence of direct dates on ore emplacement, constraints on the age of ore formation can be made from geological relationships of the geological controls on the deposits. The ores are strongly controlled by regional faults and therefore the age of ore must be as old as or younger than these faults. The structural elements are: a) the Bou Jaber diapir is located on the regional deep Tajerouine Fault; 2) the ores are located along E-W- to NE-SW-trending faulted zones including the faulted Aptian-Upper Albian unconformity) and ore-rich zones are concentrated at the intersection of the SW-NE with NW-SE faults. These tectonic elements were derived from the Miocene tectonic events of the Alpine orogeny. Thus the timing of the ore emplacement at Bou Jaber must correspond to (or possibly younger than) the Alpine orogeny in the Miocene times (Sainfeld 1956; Bouhlel 1993). Furthermore, this time of mineralization coincides well with the maximum stratigraphic burial and subsequent hydrocarbon generation and migration into the peridiapiric strata.

Sampling and analytical methods

About 100 samples of Aptian limestone, ankerite, sphalerite, galena, barite, and calcite were collected from underground, open pit exposures and drill cores. The majority of the samples were collected on the -63, -69 and -95 m levels of the mine and are representative of the A, B, and C ore bodies (Fig. 4d). Within a given ore body, minerals were collected from different zones (e.g., sulfide rich, mixed barite/sulfide and barite rich). Gypsum was obtained from Triassic evaporites outcropping on the north side of Jebel Bou Jaber and from other Triassic evaporite diapirs of the region. Mineral separates for C, O, S, Sr, Pb isotope analysis were prepared by hand-picking or by use of a dental drill.

Ore textures, mineralogy and petrographic relationships were determined on hand samples on thin and polished sections using transmitted and reflected light microscopy.

Fluid inclusion studies were carried out on a variety of minerals from the main stage of mineralization: sphalerite, barite, fluorite, and calcite. Samples were prepared as standard 200- to 500µm-thick doubly polished wafers. The measurements were carried out at the Earth Sciences Department, Faculty of Sciences of Tunis, using a Linkam THM600 freezing-heating stage on a Leitz microscope. The system was calibrated using pure CO_2 fluid inclusion (-56.6 °C), the freezing point of H_2O (0°C), and melting points of Merck standards. The precision was ±0.5°C. Fluid salinities were calculated as weight percent NaCl equivalent (wt% NaCl eq.) using the equation of Bodnar (1993). Standard procedures were carried out, with initial petrography to determine inclusion types and paragenesis in order to select material for subsequent micro-thermometric measurements. The 200 to 400µm doubly polished wafers were also examined with an epi-fluorescent microscope to observe the fluorescence of hydrocarbon-bearing inclusions.

Fluid inclusions hosted in fluorite and barite were analysed individually by LA-ICPMS. Inclusions were chosen that were clearly primary, occurring in growth zones, but in addition, fluid inclusion assemblages (FIA's) that were pseudosecondary and in some cases secondary in origin, were analysed to determine the full

range of possible fluid compositions in the ore-deposit. Individual inclusions, or groups of small related inclusions were analysed by Laser-ablation inductively-coupled mass-spectrometry (LA-ICPMS) using an Agilent 7500c mass spectrometer, combined with a Geolas ablation system. This system uses a Compex 103 ArF excimer laser with a wavelength of 193 nm and an energy density between 10 – 15 Jcm^{-2} at the sample surface. The operating frequency of the laser was typically 5Hz with spot sizes of 25µm and 50µ, the main criteria being that the size was greater than that of the inclusions. Several small inclusions could be ablated together to provide sufficient mass for analysis if inclusions were very small. The ablated material was transported from the ablation cell to an Agilent 7500c ICP-MS using 99.9999% He flowing at 2 ml min^{-1} into a cyclone mixer where it was combined with the Ar carrier gas flowing at 1.02 ml min^{-1}. The mixer prolongs the signal from the ablated inclusions and improves precision by increasing the number of cycles through the selected elements and therefore the number of determinations of their ratio relative to Na. The instrument was operated in reaction cell mode using 2.5 ml min^{-1} 99.9999% H_2 to remove interferences from ^{40}Ar on ^{40}Ca and from ^{56}ArO on ^{56}Fe. Element/Na intensity ratios were converted to weight ratios using the NIST glass standard SRM-610. For K/Na the soda lime standard SRM-1412 was used in addition to SRM-610 as it has a K/Na ratio of 1 which was closer to the analysed ratios of K/Na in barite while the K/Na ratios in fluorite are closer to the value of SRM-610. Instrumental drift was checked using SRM-610, which was insignificant over each day's analysis. Integration of the standard and sample signals used the SILLS software package (Guillong et al. 2008). Full details of the analytical protocols and calibration of the instrument are presented in Allan et al. (2005). The moderate to high salinities of the inclusions and their size enables the signal from the ablation of fluid inclusions to be easily distinguished from any matrix signal. The ablation of the host fluorite or barite precedes opening of the inclusions and continues after the inclusion signal has ceased. Therefore, any signal from the sample matrix is easily observed and can be removed by the SILLS software. The distinction between inclusion and matrix is based on the sharp rise and then decrease in the inclusion signal over a period of c. 10-15 seconds, whereas the matrix signal is more constant over the entire ablation period. In addition, areas of fluorite and barite that were free of inclusions were ablated for a total of 200 pulses to determine if they contained any significant concentrations of the elements to be determined in the inclusions. In fluorite-hosted samples there was no contamination from the matrix except for Ca and Sr in one sample. In barite there was considerable contamination from the mineral matrix for elements such as Fe, Zn, Sr, in addition to Ca and Ba from the fluid inclusion host mineral. This signal from the contamination could not be resolved from that of the fluid inclusions because it was too erratic.

Stable isotopes analyses were obtained at the U.S.G.S. Crustal Geophysics and Geochemistry Science Center stable isotope laboratory in Denver following the procedures of McCrea (1950) for carbonates and Giesemann et al. (1994) for sulfur minerals. Isotopic compositions are reported in δ–notation relative to

VPDB for carbon, VSMOW for oxygen, and VCDT for sulfur. Precision of the analyses is better than ±0.1‰ (1σ) for carbonates, ±0.2‰ for sulfur, and ±0.5‰ for oxygen in sulfates.

Strontium isotopes analyses were performed on nine barite separates and on one gypsum sample. Sample separates were finely milled, dried for four hours, than leached overnight in 6N HCl at 100°C overnight. Dry residues were dissolved in 2.5N HCl. After centrifugation, strontium was separated using standard cation exchange procedures. Sr isotopes ratios were measured on a thermal ionization mass spectrometer at the Centre Petrographique et Géochimique (CRPG), Nancy, France. Strontium deviation of analysis was usually ±0.00004.

Lead isotopes analyses were performed on galena separates selected by hand picking under a binocular microscope and then rinsed with doubly distilled water. Lead isotopes analysis were performed using the Thermal Ionization Mass spectrometry (TIMS) at the Geochronology and Isotope Geochemistry Laboratory, University of North Carolina, Chapel Hill, following the procedure described by Skaggs et al. (2012) and Garnit et al. (2012).

Results

Ore textures and mineralogy

The ore mineralogy consists of three distinct mineral assemblages representing at least three mineralizing events. (1) breccia-hosted sphalerite-galena ores with rare pyrite and some tetrahedrite micro-inclusions in galena; (2) cavity-fill barite-rich ores; (3) replacive and geodic fluorite (+ minor Pb-Zn sulfides). Post-ore calcite fills thin fractures. Alteration mineral assemblage is represented by ankerite and quartz. A generalized paragenetic sequence for the minerals at the Bou Jaber mine is given in Fig. 5.

Breccia-hosted sphalerite-galena ores (stage 1)

The sphalerite-galena ores are hosted in dissolution-collapse breccias cross-cutting the Aptian limestone strata. Breccia elements are composed of light grey Aptian limestone (2 cm to 2 m across) and are surrounded by black matrix (Fig. 6, a-c). The latter is composed of kaolinitic mudstone, minor fine-grained cubic pyrite (20 to 150 µm in size), calcite relicts, organic matter debris and abundant fine-grained hydrothermal bipyramidal quartz (100-200 µm) (Fig. 6, e-g). This black mudstone matrix is also observed in small veins and stylolites. This matrix is the main host the sulfide concentration (Fig. 6, b-c). Sphalerite occurs as honey to light brown euhedral crystals 1 to 8 mm across, with a dark brown core (Fig. 6, d-f). Galena is less abundant than sphalerite (Fig. 6, b-c) and precipitated during and after sphalerite deposition as indicated by geometric relationships and overgrowths (Fig. 6g). Minor epigenetic galena crystals, 1 to 2 cm across occur as irregular disseminations that replaced the limestone wall rock. Both sphalerite and galena contain abundant inclusions of micrite grains (up to 200 microns), bipyramidal quartz (100-200 µm), organic

matter (5-20 µm) and pyrite microcrystals (20-50 µm). These insoluble residues were inherited from the decalcification of the black matrix hosting the sulfide assemblage described below, as well from the dissolution of Aptian limestone host rocks. Bipyramidal quartz is the first hydrothermal alteration of the host rocks and pre-date sulfide deposition. Only rare barite (barite-1) aggregates have been observed in the sulfide-rich ore zones or in laterally equivalent breccias, so it seems unlikely that the sulfides replaced barite in this deposit. The black mudstone-hosted sulfides may represent limestone insoluble residue, which is common in most carbonate-hosted deposits and districts where carbonate dissolution breccias are present and commonly described as internal sediments (Sass-Gustkiewics 1996; Leach and Sangster 1993; Matlock and Misra 1993; Bouabdellah et al. 1996).

Barite- and ankerite-rich ore (stage 2)

Barite-rich ores fill hydrothermal dissolution cavities up to several meters in diameter (Fig. 7a). The wall rocks of the cavities have been partly to completely replaced by coarse-grained ankerite (ank-1) that forms 5 to 20 cm-thick halos lining the barite-rich ore bodies. Ankerite-1 occurs as aggregates of well-formed rhomohedral crystals, 1 to 5 mm across (Fig. 7b). In numerous places, the barite-rich ores consist of alternations of white and black coloured bands (Fig. 7, c-d). The black bands are composed of black mudstone similar to that described above in the sulfide stage containing fine-grained quartz-barite1-sphalerite-galena assemblage overprinted by aggregates of stage 2 ankerite (ankerite-2) which is often replaced by black fluorite-1 (see fluorite stage below). The white bands, 2 to 20 cm in thickness, are essentially composed of stacked or intergrown tabular barite crystals (barite-2), 0.5 to 3cm-thich and 2 to 20cm-long. In the central part of the barite-rich ore bodies, late-stage barite (barite-3) forms spectacular very large white to transparent barite crystals (50 cm to up to 1.5 meter-long and up 10 to 30 cm-thick) that occupie 80 to 90% of the cavities (Fig. 7e).

Fluorite (+minor sulfides) stages and post-ore calcite (stage 3)

Massive dark to black fluorite (fluorite-1), with small amounts of sphalerite and galena, most commonly fills polygonal spaces between intergrown barite crystals. In detail the fluorite-1 has partially to completely replaced the calcite and ankerite that previously cemented sulfides and barite crystals (Fig. 7f). The black-colour of this fluorite is due to abundant solid inclusions (e.g., sphalerite, micrite, ankerite, black clay, and fine-grained hydrothermal bipyramidal quartz), and to abundant oil inclusions. Following the fluorite-1 stage, fluorite-2 (with minor sulfides) forms geodic cubic crystals from few mm to 5 cm across, which are colourless or purple. This fluorite is commonly coated by rhombohedral crystals of ankerite up to 5 mm across (ank-3), and by late stage calcite occurring as large scalenoedral crystals calcite up to 5 cm across.

Post-ore spar calcite occurs in thin open fractures (5 to 20 cm wide) crosscutting the previous described ores and the host rocks.

Fluid inclusions petrography and microthermometry

Few fluid inclusions are observed in sphalerite; however barite-, fluorite-, and late-stage calcite contain numerous primary and secondary fluid inclusions suitable for fluid inclusion study. In these minerals primary fluid inclusions were identified in the context of Roedder (1984) and Goldstein and Reynolds (1994). They are classified in three types (Fig. 8): (1) Liquid water + vapour (L_w+V); (2) Liquid petroleum + Vapour (L_P+V); (3) Liquid water + Liquid petroleum + Vapour (L_W+L_P+V).

Aqueous fluid inclusions microthermometry

The microthermometric data derived from the primary fluid inclusions in sphalerite, barite, and fluorite from the Bou Jaber "Gîte de l'Est" are given in Table 1. Sphalerite contains small (5- to 20 µm size) L_w+V and L_P+V fluid inclusions. Microthermometric analysis preformed on the L_w+V inclusions yielded first melting temperature (T_{fm}) values in the range of −40° and −30 °C. The final ice melting temperatures (Tm_{ice}) vary from −18° to −13°C with a mode at −16°C. The homogenization temperatures (Th) range from 120 to 136°C with a mode at 128°C (± 5°C). Calculated salinities range from 17 to 20 wt% NaCl eq. with a mode at 19 wt% NaCl eq. (± 1%)

Transparent and geodic barite crystals (barite-2 and barite-3) contain numerous two-phase inclusions (L_W+V) (5- to 200µm size) that form locally abundant clusters. Fluid inclusions indicating stretching or necking down (Roedder 1984; Ulrich and Bodnar 1988) are not measured. It is well known that barite is susceptible to stretching of the fluid inclusions by modest heating beyond their trapping temperature (Ulrich and Bodnar 1988). Therefore, only sets of primary fluid inclusions that had the same Th values are reported. Nevertheless, there is an unknown level of uncertainty regarding the Th data for barite, consequently the reported Th values should be considered "maximum" temperatures for fluid trapping. In general the (L_W+V) inclusions present generally the same volumetric proportion of the liquid to vapour phases (L = 90 to 95 %; V = 5 to 10 %). The first melting temperature (T_{fm}) values range between about −45 to −19 °C (ave. −34±7°C, n=36). The final ice melting temperatures (Tm_{ice}) range from −14 to −8°C (ave. −10±1°C; n=31). The homogenization temperatures (Th) range from 100 to 130°C (ave. 114±10°C). Calculated salinities range from 11 to 15 wt% NaCl eq. (ave. 13 wt% NaCl eq. ± 1%).

Fluorite-1 and fluorite-2 samples contain abundant two-phase inclusions (L_W+V) (5- to 200µm size). The T_{fm} recorded temperatures range from −45° to −28°C. The final ice melting temperature (T_{mi}) values vary from −20° to −12 °C with a mode of −17°C. The homogenization temperatures range from 140°to 165°C

(mean = 152±7°C). Calculated salinities range from 16 to 23 wt% NaCl eq. with a mean =20±1.5 wt% NaCl eq.

Transparent late-stage calcite crystals (calcite-2), overlapping fluorite in druses and caves, contain small but numerous two-phase inclusions (L_W+V) of about 5- to 50- µm size. The first melting temperature (T_{fm}) values range between −33 to −30 °C. The final ice melting temperatures (Tm_{ice}) were in the range of −18° to −15.5°C with a mode of −17°C. The homogenization temperatures (Th) range from 109° to 117°C (ave. 114±2°C). Calculated salinities range from 19 to 21 wt% NaCl eq., with a mode of 20 wt% NaCl eq.

Petroleum fluid inclusions

Liquid hydrocarbon fluid inclusions are observed in sphalerite and are abundant in fluorite. The inclusions in sphalerite are less than 5 to 10µm in size. Large inclusions (80 to 200 µm) are observed in the core- or along growth zones of fluorite crystals. In black fluorite crystals, petroleum-bearing inclusions represent more than 30% of the total inclusions. The black coloured fluorite is due to petroleum inclusion abundances.

Two types of primary fluid inclusions are observed: L_p+V and L_W+L_P+V fluid inclusions that are isolated or distributed along growth zones. These inclusions may coexist in the same mineral zones with aqueous inclusions (L_w+V). Secondary L_w+V and L_P+V fluid inclusions are located along fractures, cracks and cleavage planes. In transmitted light, liquid hydrocarbon inclusions are usually brown- to yellow-colored. In epifluorescence observations, most of the hydrocarbon inclusions show fluorescence emissions in the light yellow to light or deep blue colours.

Primary L_p+V inclusions recorded homogenization temperatures that range between 97° to 140°C, and are lower than the Th values of coexisting aqueous inclusions (100° to 165°C). The differences in homogenization temperatures are about 20°C which probably reflects differences in pressure corrections caused by the greater compressibility of oil than water (Roedder 1963).

Semi-quantitative compositions of hydrocarbon inclusions trapped in barite and fluorite crystals were determined by infrared microscopy and microfluorometry, as described in Guilhaumou et al. (1990). Both techniques show the presence of aliphatic and aromatic components in the oil, but microfluorometry shows that in barite the components are aliphatic dominant and in fluorite aromatic compounds dominate. The transition from aliphatic-rich oil inclusions to more aromatic components correlates with the timing and temperature of barite to fluorite depositions. The temperatures associated with the deposition of barite are low at around 100° to 130°C, whereas in fluorite the temperature is higher at around 140° to 165°C. In addition, fluorite, being paragenetically later than barite indicates there was more time for the oil to mature.

Homogenization temperatures-salinity relationships

Salinities and homogenization temperatures from primary fluid inclusions (L_w+V) in sphalerite, barite, fluorite and calcite are shown in Fig. 9. The data indicate that sphalerite, barite, fluorite, and late stage calcite were probably deposited from fluids with homogenization temperatures of between 100 to 165°C (ave. 130°C±18°C) and salinities in the range of 11 to 22 wt% NaCl eq. (ave. 17.5±3 wt% NaCl eq.).

Based on the mineral paragenesis and the defined mineralization stages, the brine fluids are of three types: (1) the fluid that deposited sphalerite (A fluid) is characterized by high salinities (17 to 24 wt% NaCl eq.), and homogenization temperatures (112° to 136°C); (2) the fluid responsible for barite deposition (B fluid) is characterized by low salinities(11 to 17 wt% NaCl eq.), and low temperatures (Th = 100° to 130°C); (3) fluorite was deposited by fluids (C fluid) with salinities ranging from 19 to 21 wt% NaCl eq. (ave. 20%), and relatively high homogenization temperatures of 140° to 165°C; and (4) late-stage calcite was deposited by a fluid (D fluid) with Th raging from 109° to 117°C and calculated salinities between 19 to 21 wt% NaCl eq. (mode at 20 wt% NaCl eq). The mean temperatures of the ore fluids decreased from sphalerite (125°C) to barite (115°C) and increased during fluorite deposition (152°C); then decreased to ~110°C during the late stage calcite precipitation.

Composition of fluid inclusions using LA-ICPMS

Approximately 200 fluid inclusions hosted in fluorite and barite were analysed individually by LA-ICPMS. A summary of the element/Na weight ratios for individual fluid inclusions and their reproducibility (based on more than 30 measurements for each sample) is presented in Table 2. The average weight ratios have also been converted to elemental concentrations (ppm) based on the average salinity of the inclusions in fluorite (18 equiv. wt% NaCl) and barite (13 equiv. wt% NaCl) determined by microthermometry (Banks et al. 2000). The accuracy of the calculation relies on the ability to measure all of the cation/Na ratios in the inclusion which are impossible for Ca and Ba because these are the cation in the host mineral. In fluorite it was possible to estimate the Ca/Na ratio from the ice and hydrohalite melting temperatures and using the NaCl-$CaCl_2$-H_2O phase diagram to calculate the Na/Ca ratio, which was found to be approximately 0.5. In barite, Ca is present as $CaCO_3$and CaF_2solid inclusions in the mineral matrix and contaminates the fluid analyses. It was also not possible to observe the ice-hydrohalite melting relationship in these inclusions; therefore it was not possible to directly estimate the Ca/Na ratio of these inclusions. Based on similarities between other elements in fluorite and barite hosted inclusions, we assume the Ca/Na ratio to be similar to that in fluorite. In the barite the ratios of Ba, Zn, and Sr to Na were also unreasonable high and were clearly from contamination in the host mineral.

The fluid inclusions in fluorite are dominated by Na>Ca>K>Mg, with the concentrations of Sr, Fe and Zn each being equivalent to that of Mg. Concentrations of ore metals such as Cu are 250 to 450 ppm, Zn 850

to 2100 ppm, and Pb150 to 430 ppm. The difference in the concentrations between the different fluorite-hosted fluids are, in the majority of cases, statistically significant and not due to the precision of the replicate analyses. The composition of the major cations in the barite-hosted inclusions are different to those in fluorite. These are dominated by K>Na>Ca>Mg, with Cu and Pb at significantly lower concentrations than in fluorite. Due largely to the different K/Na ratios, bivariate plots of pairs of individual inclusions analyses (Fig. 10, a-l) show there are 2 distinct fluid compositions, whereas other ratios, such as Mg, Li, Sr, Cu, Pb and Mn/Na are broadly similar. The elemental ratios of the 3 fluorite samples largely overlap indicating a common fluid. Differences in the Mg/Na and K/Na between samples BJ9612 and the other samples are real but not significant enough to indicate these inclusions contain another distinct fluid.

Isotope geochemistry

Carbon and oxygen isotopes in carbonates

The isotopic results for barren Aptian limestone (n=4), mineralized limestone (n=9), ore ankerite (n=8) and post ore calcite (n=18) are listed in Table 3 and shown on Fig. 11.

The limestone have $\delta^{13}C$ values ranging from -2 to 3.9 ‰ and $\delta^{18}O$ values ranging from 26.2 to 30.1‰, within the ranges typical of marine limestones of Cretaceous age (Veizer and Hoefs 1976; Land 1980). The values are comparable to values reported for Aptian limestones elsewhere in Central Tunisia and eastern Algeria (M'Rabet1987; Bouzenoune and Lecolle1997).

Ankerite-1 (n=3) which precipitated after the sulphide stage and before barite, has $\delta^{13}C$ values of 2.7 to 3.6‰ and $\delta^{18}O$ values of 26.8 to 26.9‰. Ankerite-2 (n=3), which precipitated after barite, has $\delta^{13}C$ values of 2.4 to 3.6 ‰ and $\delta^{18}O$ values of 26 to 27 ‰. Ankerite-3 (n=3), which precipitated in geodes after fluorite, has $\delta^{13}C$ values of -0.5 to 1.5‰ and $\delta^{18}O$ values of 19.6 to +22.9‰.

Five samples of early calcites (calcite-1), which precipitated in geodes after fluorite-2 and ank-3, have $\delta^{13}C$ values of 1.3 to 3.8‰ and $\delta^{18}O$ values of 18.8 to +23.1‰. Late calcite (calcite-2) (n=11) has $\delta^{13}C$ values of 2.6 to 6.2 ‰ and $\delta^{18}O$ values of 24.8 to 27.4‰. Calcite-2 occurs in late thin fractures and appears to be precipitated after the end of the mineralized hydrothermal system.

The pre-barite ankerite (ankerite-1) and post-barite ankerite (ankerite-2) show similar ranges of $\delta^{18}O$ values, 26.8–26.9 ‰ and 26–27 ‰, respectively, isotopically similar to the lowest $\delta^{18}O$ Aptian limestone (26.2–30.1‰); whereas the fluorite–ankerite-3 –calcite-1 sequence contains the ankerite and calcite with lower $\delta^{18}O$ values, 18.8–23.1‰ and 19.6–22.9‰, respectively, although there is greater isotopic variation in the hydrothermal carbonates (ankerite-1,2,3 and calcite-1) (18–27‰) than in the Aptian limestones (26.2–30.1‰) (Fig.11).

548 The $\delta^{13}C$ values of host limestones and hydrothermal ankerites are quite uniform: 2.0±1.9‰ for the
549 limestones, 3.1±0.5‰ for pre-barite ankerite, 2.6±0.3‰ for post-barite ankerite, and 0.5±1‰ for post-fluorite
550 ankerite. The isotopic similarity indicates that carbon in all three ankerite generations was derived from the
551 local Aptian limestones, and that carbon isotopic equilibrium was established between hydrothermal fluids
552 and the host limestones during the main stages of ankerite and sulfide precipitation. Late stage calcite shows
553 higher $\delta^{13}C$ values (3.6±1‰).
554 Oxygen isotopic compositions of limestone host rock are restricted to a narrower range (26.2–30.1‰)
555 than the hydrothermal ankerite and calcite generations (19.6–27.4‰). The limestones represent the
556 isotopically heaviest carbonates. The $\delta^{18}O$ values of carbonates display a general downward trend in the
557 following sequence: limestone (26.2–30.1‰) → pre-barite ankerite (26.8–26.9‰) ≈ post-barite ankerite
558 (26.8–26.9‰) → post-fluorite ankerite (19.6–22.9‰) ≈ post-fluorite calcite (18.8–23.1‰). This trend
559 resembles similar trends that have been observed at other MVT deposits (e.g., Frank and Lohmann 1986;
560 Nesbitt and Muehlenbachs 1994; Spangenberg et al.1996) in which isotopically lighter O is seen in
561 paragenetically late carbonates compared to the unaltered host carbonates. The carbonates exhibit a positive
562 covariation in a $\delta^{13}C$ vs $\delta^{18}O$ plot.

563 Sulfur isotope characteristics in sulfides and sulfates

564 Sulfur isotopic compositions were determined on 18 sphalerite, 43 galena, 3 pyrite, 45 barite and 22 gypsum
565 samples (Table 4, Fig.12).The pyrites have $\delta^{34}S$ values of about 16‰, and sphalerites range from 8.4 to
566 9.8‰. There are no significant differences in sphalerite compositions among different sampled ore bodies, or
567 within ore zones in a single ore body, or even among sulfide stages. Galenas associated with the analyzed
568 sphalerites range from 1.1 to 9.6‰. Most of the galena $\delta^{34}S$ values occupy a narrow interval between 5 and
569 6‰. There is no significant difference between the galena that replaced the breccia matrix in dissolution
570 cavities-type ores (1.1–8.2‰; ave. 5.7‰), and epigenetic galena porphyroblasts in the host rocks or galena
571 associated with the fluorite stage event (3.2–9.6 ‰; ave. 6.6‰).
572 The $\delta^{34}S$ values of Triassic gypsum range from 13.4 to 17.0‰ (ave. 15‰, n=12) similar to previously
573 reported compositions for Triassic gypsum of the Diapir Belt (Sheppard et al. 1996; Salmi-Laouar et al.
574 2007). These values match the $\delta^{34}S$ values of Triassic seawater (13–16‰) (Claypool et al. 1980;
575 Kampschulte and Strauss 2004).
576 The $\delta^{34}S$ values of barite range from 18.4 to 24.5‰ (ave. 22‰, n=45) (Table 4, Fig. 12, a-b). Despite
577 their wide spatial distribution, either within a single ore body or throughout the three ore bodies, the barites
578 show a relatively narrow range of $\delta^{34}S$ values.

579 Oxygen isotope characteristics in sulfate minerals

580 The $\delta^{18}O$ values for Triassic gypsum range from 13 to 16‰, in good agreement with the $\delta^{18}O$ value of marine
581 sulfate in Triassic time (Claypool et al. 1980). The $\delta^{18}O$ values of barites vary between 19.6 and 23.5‰ (ave.
582 22‰, n=13). The higher values imply that barite did not form simply by dissolution and re-precipitation of
583 Triassic evaporite minerals. In fact, the barite $\delta^{18}O$ values are higher than the value of marine sulfate of any
584 age (Claypool et al. 1980). Thus, rather than reflecting the source of the sulfate, the values reflect either
585 isotopic exchange, possibly involving oxygen exchange with H_2O driven by hydrothermal heating, or a
586 reservoir effect associated with partial reduction of a fixed sulfate pool.

587 **Radiogenic isotopes**

588 $^{87}Sr/^{86}Sr$ ratio in barite and gypsum

589 In order to constrain the origin of high-barium fluids and to monitor possible changes in fluid composition
590 during barite deposition, nine samples of barite from the main barite stages were selected for $^{87}Sr/^{86}Sr$
591 analysis. In addition one sample of anhydrite from the Triassic diapir was analysed. Results of the $^{87}Sr/^{86}Sr$
592 analysis are listed in Table 5 and presented on Fig. 13. Regional $^{87}Sr/^{86}Sr$ ratios for Cretaceous sediments
593 (Calvez et al. 1986) are also shown for comparison. A slight trend of ^{87}Sr-enrichment is observed from early
594 to late generations of barite crystals. This trend indicates extensive exchange reactions between hydrothermal
595 fluids and source rocks. A similar trend was observed in calcite generations in carbonate-hosted Pb-Zn
596 deposits (Lange et al. 1983; Spangenberg et al. 1996).

597 Bou Jaber barites show Sr isotope compositions ranging from 0.709821 to 0.711408; these values are
598 radiogenic compared to Triassic anhydrite with a $^{87}Sr/^{86}Sr$ ratio of 0.70800, whichis close to the estimated
599 ratio for seawater during Triassic times (0.7073−0.7080; Veizer and Compston 1974; Burke et al. 1982). The
600 barite Sr-isotopes values are also more radiogenic than the Tunisian Cretaceous sediments (0.707400 to
601 0.707600; Orgeval 1994) that are close to the ratios of 0.70730 to 0.70750 for Cretaceous seawater
602 (Koepenick et al. 1985). The radiogenic strontium of the Bou Jaber barite might reflect leaching of a feldspar-
603 rich reservoir containing rocks and/or rubidium-rich minerals

604 Lead isotopes

605 Sixteen samples of galena were collected from the Bou Jaber ore deposit for lead isotope analysis. Results are
606 presented in Table 6 and plotted in Fig. 14, and are compared to fields of sulfide lead compositions from 24
607 Tunisian Pb-Zn deposits of the Tell thrust zone and the Atlas Foreland (Bouhlel et al. 2013) and to the Pb-
608 isotope compositions of a 15 Ma biotite microgranite sample from the Nefza region (Decrée 2008) and from

609 the Galite island in the Tunisian offshore (Juteau et al. 1986), about 120 Km and 150 km north of Bou Jaber
610 area, respectively (Fig. 1).

611 Bou Jaber galenas have $^{206}Pb/^{204}Pb$, $^{207}Pb/^{204}Pb$, and $^{208}Pb/^{204}Pb$ values ranging from 18.697–18.786 (ave.
612 18.729), 15.643–15.762 (ave. 15.679), and 38.7057–39.228 (ave. 38.842) respectively. Results show
613 remarkable homogeneity of lead isotope compositions that plot within a narrow field, indicating a single or
614 homogenous source and suggesting a short duration of the mineralization event.

615 Lead isotope compositions form an elliptic field in both $^{207}Pb/^{204}Pb$ versus $^{206}Pb/^{204}Pb$ and $^{208}Pb/^{204}Pb$
616 versus $^{206}Pb/^{204}Pb$ plots. The majority of the analyzed galena samples plot in a field below the upper crust
617 evolution curve in the orogenic plot (Fig.14a) and above the orogen curve (Fig. 14b) indicating the
618 dominance of continental crustal sources. In the orogenic plot, some of the galena samples plot clearly above
619 the upper crust curve (i.e. high μ), indicating a large component of a radiogenic source. Some others plot
620 below the upper crust curve (i.e. low μ), indicating a large component of non-radiogenic sources. The lead
621 field of Bou Jaber lies within the lead isotope field defined by the major Tunisian Pb-Zn deposits (Bouhlel et
622 al. 2013).

623 Given the homogenous Pb-isotopic compositions of the Bou Jaber galena samples, it is reasonable to
624 propose that the Bou Jaber ores were formed from fluids that passed through the same well-mixed source
625 rock (s) over a relatively restricted period of time. Bou Jaber is located on the SW-NE-trending Tajerouine
626 Fault (Fig. 1), reflecting the main Paleozoic-basement structural features that enabled diapirism and probably
627 influenced fluid migration. It is possible that the lead may have been extracted from the basement or from
628 siliciclastic feldspar-rich rocks in the basin, consistent with the $^{87}Sr/^{86}Sr$ ratios in barite.

629 The Pb-Zn isotopic lead field also overlaps that of the Miocene felsic rocks of the Galite Island and the
630 Nefza region. These rocks, related to Miocene anatexis, were derived from a metaluminous basement
631 (Belayouni et al. 2010). This feature may indicate that the ore lead and the felsic rocks were originally from
632 similar source rocks, and/or probably extracted at the same period.

633 The Bou Jaber galena samples give $^{207}Pb/^{206}Pb$ model ages from the plumbotectonic model of Zartman
634 and Doe (1981), between 400 and 300 Ma (Fig. 14a), older than the proposed Miocene age of the Atlassic
635 metallognic events (Sainfeld 1956; Rouvier et al. 1985; Bouhlel 2005). This retardation which is was also
636 observed for the Miocene felsic rocks (Decrée 2008) may be due to the contribution of a less radiogenic
637 material with low uranium content such as the lower crust).

638 **Discussion**

639 The Bou Jaber Ba-F-Pb-Zn deposit is located adjacent to a Triassic salt diapir in the Salt Diapir Belt (Fig 1).
640 Although there are more than 100 diapirs in this belt, only a relatively few have spatially associated economic
641 ore deposits. The diapir-related ore deposits in the Salt Diapir Belt contain three distinct ore assemblages

642 dominated by sphalerite and galena, barite, or fluorite. Some deposits like Bou Jaber contain ores of all three
643 assemblages (Fig. 1) whereas others contain only one assemblage (i.e., Bou Grine with sphalerite and galena;
644 Bouhlel et al. 2009). The presence of the three paragenetically distinct ore assemblages in a single diapiric
645 zone at Bou Jaber provides an opportunity to better understand how if at all, these mineral assemblages may
646 be related and insights into regional controls on the Zn-Pb-barite-fluorite mineralization.

647 Comparison to similar ores of the world

648 Until the recent studies at the giant Jinding diapir-hosted deposit in China (Leach et al. 2013), the resources
649 of diapir-related Zn-Pb ores were considered to be relatively small as well as uncommon relative to the
650 abundance of diapirs worldwide. Other than Jinding) the most significant diapir related ores were at the Bou
651 Grine Zn-Pb deposit (about 7 million tons 12% combined Zn+Pb). Other well-known diapir related
652 mineralization is also known from the Gulf Coast, United States with the Hockley Dome being well studied
653 (e.g., Kyle and Posey, 1991 and references therein). Due to the relatively small number of mineralized diapir-
654 related ores, there are few observations and data about the fundamental ore controls.
655 The new data presented here show that the diapir-related Bou Jaber lead-zinc ores have many geological,
656 textural and geochemical features of MVT lead-zinc ore deposits (e.g., Sverjenski 1986; Leach et al. 2005).
657 However, the presence of coeval barite or fluorite with the Zn-Pb ores is rare in MVT ores (e.g., Leach and
658 Sangster 1993; Leach et al. 2005). Where minor barite does occur in MVT ores, it is either early or late in the
659 paragenetic sequence and typically has distinctly different sulphur isotopic compositions from sulfide
660 minerals and different fluid inclusion compositions from associated sulfide- or gangue minerals, consistent
661 with different mineralizing events (e.g., Leach et al. 2005).In the giant Ozark MVT province in the
662 midcontinent of the United States, the world-class Southeast Missouri Zn-Pb district is devoid of barite or
663 fluorite occurrences. However, large barite deposits in the region formed from compositionally distinct fluids
664 and the ores are stratigraphically, spatially and temporally distinct. Ore fluids that transport and deposit MVT
665 or Clastic Dominated (CD) Zn-Pb ores can contain oxidized sulphur (and insignificant amounts of reduced
666 sulfur) that significantly limits Ba transport with significant sulphate (Cooke et al. 2000). Barite and or
667 celestite are present in minor amounts in the Hockley-, and Jinding Pb-Zn mineralization, however the barite
668 in these ores is interpreted to represent separate events related to the diagenetic transformation of the original
669 gypsum/anhydrite and not directly with Zn-Pb mineralization. In view of the world occurrences of
670 mineralized diapirs, the presence of abundant barite and fluorite in the Tunisian Salt Diapir Belt is unusual.
671 Perhaps the best examples of coeval fluorite with carbonate-hosted Zn-Pb mineralization are the fluorite-
672 dominated districts of southern Illinois and Central Kentucky of the United States. These deposits have been
673 considered a sub-type of a larger family of MVT ores because they are commonly associated with continental
674 rifts and are suspected of being related to a magmatic component of fluorine that mixed with basinal brines
675 (Plumlee et al.1994; Leach and Sangster 1993, Kendrick et al. 2002; Leach, et al. 2005). A late fluorite-barite

assemblage overprints the main Zn-Pb MVT event in the Central Tennessee MVT district but this is likely to be related to the nearby Illinois fluorite event. There are many small Zn-Pb MVT ores in France and a few deposits have a late fluorite event, which is considered to represent an event superimposed on an older Zn-Pb event (Macquar et al. 1990).

Other than the Bou Jaber deposit, fluorite is not present in the Pb-Zn rich ore bearing diapirs either in Tunisia (e.g. Bou Grine, Fedj el Adoum) or in China (Jinding) nor is it reported from the Gulf Coast diapirs. Fluorite-rich diapirs, low in Zn-Pb mineralization are known both in Tunisia (e.g., the Zaghouan district; Bouhlel 1982; Bouhlel et al. 1988) and Morocco (e.g., Tirremi; Bouabdellah et al. 2013). However, a fluorite + barite (low Zn-Pb) ± calcite-dolomite-quartz mineral assemblage is more common in some vein deposits (e.g., U.S. Central Tennessee, Leach and Sangster, 1993); Zaghouan district, Tunisia, Bouhlel 1982; Bouhlel 1985; Bouhlel et al. 1988) and the Cevennes area, France; Macquar et al. 1990), particularly where basement-connected vein deposits cut the cover rock sequences.

Evidence for separate mineralizing events at Bou Jaber

The Bou Jaber ores display three mineral assemblages that are spatially and temporary distinct: (1) Pb-Zn sulfides within breccia bodies; (2) barite with early minor sulfides in dissolution cavities, (3) fluorite ores with minor sulfides that invade and crosscut the sulfide and barite ores and (4) three distinct fluids as shown from the mineral paragenesis and fluid inclusion microthermometry. Figure 5 shows the paragenetic relations of these three events: the main stage of sphalerite and galena was followed by the barite event and finally by the fluorite event. The combined fluid inclusion temperature-salinity plot (Fig. 10) clearly shows three distinct groups based on salinities and temperatures for sphalerite, barite and fluorite: a higher temperature-salinity field for fluorite, lower temperature-salinity field for barite and an intermediate field for sphalerite. Although this distribution could possibly be interpreted as a cooling and dilution trend of a single fluid, the LA-ICPMS analyses show the fluid inclusions in barite and fluorite have two different fluid compositions; no data are available on sphalerite. Inclusions in fluorite are metal-rich (100's to 1000's ppm Pb, Zn, Cu, Fe) but the inclusions in barite are metal-deficient. Bi-variant plots of pairs of individual inclusions analyses (Fig. 10, a-l) show there are 2 distinct fluid compositions based largely on the different K/Na ratios while other ratios, such as Mg, Li, Sr, Cu, Pb and Mn/Na are broadly similar.

Source of the ore fluids

The origin of high salinity brines that form sediment-hosted Zn-Pb ores is generally attributed to evaporated seawater with or without involving some minor amount of dissolved halite. Although information on the composition of ore fluids in diapir-related ores are scarce, data for two diapir-related metallic deposits, the Orduña-Murgía deposits in Basque-Cantabrian basin Northern Spain (Grandia et al. 2003) and the Jbel

Tirremi fluorite-barite deposit in Morocco (Bouabdellah et al. 2013) show the ore fluids were dominated by high salinity brines representing a mixture of evaporated seawater and dissolved halite.

Unfortunately, there are no data on the composition of the Zn-Pb ore fluids other than the fluid salinity from the fluid inclusions. Therefore, nothing can be concluded about the origin of the Zn-Pb fluids other then they plot in a temperature-salinity space (Fig. 9) that differs from the fluorite and barite fluids. Inclusions in fluorite from the Bou Jaber deposit have Cl/Br and Na/Br ratios of several thousand, consistent with dissolution of halite whereas the inclusions analysed in barite have values lower than those of seawater which are indicative of a Br-enriched brine derived from the evaporation of seawater plus a component of halite dissolution. The Bou Jaber fluorite ore fluids are Na-Ca dominated with low Mg concentrations indicating significant dolomitization of limestone by the fluids. The salinity of the barite fluids could be the result of evaporation of seawater prior to halite saturation or by the dilution of a more saline fluid with meteoric water. Furthermore, the higher K/Na values of fluid inclusions from barite suggest the brines interacted with K-rich rocks in the basement or in siliciclastic sediments in the basin. Oxygen isotope compositions of the ore fluid calculated from late stage calcite indicate that the $\delta^{18}O$ of the fluid varied between ≈ +3 and ≈ +8‰. Such a fluid most likely originated from formation waters in isotopic equilibrium with the host rocks. The oxygen isotopic composition of the fluids that deposited the Bou Jaber Ba-F-Pb-Zn ores are similar to that of modern sedimentary basinal brines and MVT deposits (e.g., Mc Limans 1975; Mc Limans1977) as well as in the nearby Fedj el Adoum deposit (Charef and Sheppard 1987).

Sources of the metals

The sources of metals in sediment-hosted ores are poorly understood. An extensive analysis of lead isotopes from sediment-hosted Zn-Pb ores (Leach et al. 2005) concluded that no single host rock type could explain the lead isotopic compositions of galena in the deposits. In many examples, the lead isotopic compositions of the ores suggest that the ore fluids may have interacted with the basement rock, the weathered regolith or basal sandstones or with detritus in the sediment cover rocks that contains material weathered from the basement rocks.

Interpretations of the lead isotope data from Bou Jaber indicates that the lead was derived from upper crustal rocks and it is reasonable to assume that these rocks were also the source of Zn, Fe and Ba. In Figure 14, the isotopic data for Bou Jaber lies within the large field defined by Pb-Zn deposits of the Tell Thrust Belt and the Atlas Foreland. These regions have the same Paleozoic basement rocks, which suggest that the basement rocks or sediment derived from the basement may have contributed metals in both regions. This suggestion is consistent with compilations of lead isotopes compositions from global MVT ores (Leach et al., 2005) that suggest a relationship between the isotopic compositions of ores in the district and the compositions of the basement rocks.

741 Bou Jaber barites have Sr isotope compositions that are radiogenic compared to Triassic anhydrite or the
742 estimated ratio for seawater during the Triassic and are also more radiogenic than the marine Tunisian
743 Cretaceous sediments. The most likely source for the more radiogenic strontium in the barite is feldspar-rich
744 rocks and/or Rb-rich minerals.
745 The possible sources for fluorine are problematic. The common spatial association of world fluorite
746 deposits with continental rift basins leads to the speculation that fluorine was possibly derived from deep-
747 seated basement sources (i.e., mantle gases as in the Illinois fluorite district; Plumlee et al. 1994; Kendrick et
748 al. 2002). This suggestion is consistent with the abundance of fluorite deposits adjacent to Mio-Pliocene
749 graben structures in the Tunisian Atlas Foreland (Fig. 1). Note that Bou Jaber lies along the border of the one
750 of these grabens at the intersection with a salt diapir.

751 Sources of Sulfur

752 Based simply on proximity, gypsum in the nearby Triassic evaporite diapirs is the most obvious sulfur source
753 for the Bou Jaber ores. However, sulfate minerals or sulfate-bearing formation waters within overlying,
754 younger strata would also be plausible sources inasmuch as ore formation did not occur until Miocene-
755 Pliocene time.
756 The reduced sulfur in sphalerite and galena was most likely produced by thermochemical sulfate
757 reduction (TSR). The evidence supporting this interpretation is two-fold. First, the minerals show relatively
758 narrow isotopic ranges and relatively high $\delta^{34}S$ values compared with the ranges and values that commonly
759 result from bacterial sulfate reduction (BSR) in marine sediments or marine rocks (Machel et al. 1995).
760 Second, the fluid inclusion microthermometry indicates that temperatures were sufficient to drive abiotic
761 reactions between sulfate and organic matter (80–100<T<150–200°C, Machel et al. 1995), the presence of
762 which is confirmed by organic inclusions in sphalerite. Additional evidence for favourable temperatures for
763 TSR are found in the isotopic results for 13 sphalerite-galena pairs, which yield consistent isotopic
764 equilibration temperatures in the range 118–200°C (Table 4).
765 The mean $\delta^{34}S$ values for sphalerite and galena, 9 and 6‰, respectively, are 6–9‰ lower than the average
766 value for the Triassic evaporites (15‰, Table 4). The offset in values is smaller than the kinetic isotope effect
767 associated with TSR (–10 to –20‰; Machel et al. 1995), which implies that TSR consumed a substantial
768 fraction of the available sulfate causing the isotope effect to be only partly preserved (Machel et al. 1995).
769 Thermochemical reduction of younger marine sulfate would also be compatible with the data. For example,
770 the isotopic offset of sphalerite and galena from marine sulfate of Miocene age ($\delta^{34}S$~22‰; Paytan et al.
771 1998) would be 13–16‰, consistent with the full expression of the kinetic isotope effect.
772 The mean $\delta^{34}S$ value for barite (22‰) matches Miocene marine sulfate (~22‰) better than Triassic
773 gypsum (~15‰, Table 4), but the Triassic cap rock is more likely to have been the source of barite sulfate.

774 The supporting evidence can be seen in a plot of $\delta^{34}S$ versus $\delta^{18}O$ (Fig. 12), which shows that the barite data
775 extend toward the measured composition of Triassic gypsum rather than the composition of Miocene marine
776 sulfate ($\delta^{34}S$~22‰, $\delta^{18}O$~11‰; Paytan et al. 1998; Turchyn and Schrag 2004). The colinearity of gypsum
777 and barite strongly suggests that Triassic cap rock was the source of sulfate for barite formation and that the
778 sulfate was isotopically modified by sulfate-consuming chemical reactions and possibly also by oxygen
779 isotopic exchange reactions. Qualitatively, the isotopic modifications are what would be expected where TSR
780 operated under conditions of limited sulfate supply, the increase in $\delta^{34}S$ reflecting the kinetically-controlled
781 preferential reduction of ^{34}S-depleted sulfate and the increase in $\delta^{18}O$ reflecting either preferential reduction
782 of ^{18}O-depleted sulfate or thermally-driven oxygen exchange between sulfate (or reduction intermediates) and
783 H_2O. In that they show effects consistent with TSR under conditions of limited sulfate supply, the isotopic
784 compositions suggest that barite may have formed from sulfate that remained at the site of ore formation after
785 sphalerite and galena had precipitated. Thus, the simplest interpretation of the data is that Triassic evaporites
786 furnished sulfur for both the sulfide and the barite event.

787 Processes of ore deposition

788 Sphalerite-galena stage: At the temperatures of ore deposition in the diapiric zone of a carbonate-rich
789 sequence, ore-forming concentrations of Zn and Pb are possible in brine where the ratio of sulfate to reduced
790 sulfur is very high. The deposition of the sphalerite-galena assemblage was most likely achieved by mixing
791 this metal-bearing brine from deep in the basin with a reservoir of reduced sulfur already present in the diapir
792 area. In this scenario, TSR processes involving organic matter in the diapir rocks had reduced sulfate in the
793 diapir or in the fluids residing in the peridiapiric strata prior to the influx of the metaliferous brines. It is
794 possible that some TSR processes may have contributed to the reduced sulfur budget by in situ TSR of sulfate
795 in the inbound metaliferous fluid by local organic matter. Mixing processes of a metal-rich brine with reduced
796 sulfur not only precipitates sulfides but also generates large amounts of acid that must be buffered by the
797 carbonate host rocks. This process is shown by the abundance of dissolution breccia and collapse-breccia,
798 caves, and enhanced pore space, host rock replacements and extensive vuggy porosity in the host rocks.
799 Cooling of the ore fluid, as suggested by the cristallization of fine-grained bipyramidal quartz, may have also
800 contributed to the precipitation of sulfides, but to a lesser degree.

801 Barite stage: The previous discussion of sulfur isotopes show that the colinearity of sulfur isotopes for
802 gypsum and barite strongly suggests that Triassic cap rock was the source of sulfate for barite formation and
803 that the sulfate was isotopically modified by sulfate-consuming chemical reactions (i.e., TSR) and possibly
804 also by oxygen isotopic exchange reactions. Therefore, barite deposition must have been produced when a
805 Ba-rich fluid with low Zn, Pb and perhaps with high-reduced sulfur mixed with the sulfate brine in the area of

806 the diapir. Acid is also produced in this reaction that also led to the concurrent dissolution of the carbonate
807 host rocks.

808 Fluorite stage (+minor Pb-Zn sulfide): The high temperature of fluids responsible for fluorite deposition, and
809 the dominance of a Na-rich fluid derived from the dissolution of halite are permissive for the formation of
810 CaF- complexes. The high temperatures also account for the high metal contents measured in the fluid
811 inclusions. At high temperatures, some reduced sulfur can be transported together with Zn and Pb (Yardley
812 2005). A fluid with this metal load and fluorine transport as a CaF complex can deposit fluorite together with
813 sphalerite and galena simply by cooling and fluid dilution.

814 **Timing of mineralization, structural controls, tectonic triggers and fluid migration**

815 It is clear that multiple fluid reservoirs that include hydrocarbon-bearing fluids, evaporated seawater, halite
816 dissolution brines as well as a presumed meteoric component were involved in the three distinct ore events at
817 Bou Jaber (Fig. 14). The interactions of these fluids with other fluid reservoirs containing reduced sulfur
818 (H_2S) or oxidized sulphur (SO_4) were essential to precipitate sulfides and barite. Assuming the evaporated
819 seawater component formed during the deposition of the Triassic evaporites, these very dense and low
820 viscosity brines probably migrated into the deep parts of the basin, including the Palaeozoic basement rocks.
821 Given that fluid mixing was likely an important depositional process, the ascent of the dense, deep basinal
822 fluid into upper stratigraphic levels required exceptional hydrological events. Although hydrological
823 modelling of fluids in and about salt diapirs show complex fluid regimes such as thermohaline and density
824 convection, release of geopressured fluids and focusing of fluids along impermeable evaporites and diapiric
825 structures (e.g., Kyle and Price 1986; Evans et al. 1991), we suggest that normal basin and diapir-controlled
826 fluid migration was not singularly responsible for ore deposition. If the Tunisian diapir-related ores formed
827 from normal basin processes involving diapirs, then we would expect that there should be many more diapiric
828 related ore deposits in the Tunisia Diapir Belt as well as in the Tethyan diapirs of Central Algeria- and
829 Western Morocco parts of North Africa, as well as in Europe and other diapirs provinces in the world.
830 There is an increasing appreciation that major sediment-hosted Zn-Pb ores ore formed as a result of large-
831 scale tectonic triggers (Leach et al. 2010) that released deep-seated fluids into favourable geochemical traps.
832 This may be the situation for Bou Jaber and the other ore deposits of the Tunisia salt diapir belt. The first
833 significant tectonic event after evaporite formation was mid-Cretaceous rifting during the Africa-Europe plate
834 separation that produced tilted blocks, half-grabens and salt diapirism. There is no evidence for ore
835 emplacement during this tectonic and diapirism period. However we suspect that the compressional event in
836 mid-Miocene (Rouvier 1977) related to the African European plates subduction-collision that produced
837 thrusting, SW-NE-trending folds and the return of salt diapirism, may have been the tectonic trigger that
838 brought deep-seated brines into the upper parts of the diapir body and into the peridiapiric cover rocks. The

ascent of deep-seated Zn-Pb brines would have interacted sources of reduced sulfur and hydrocarbons and precipitated the main-stage sphalerite and galena ores.

The diapirs may have focused fluid flow along the southeast flanks of the diapirs that define the Alpine thrusting. Diapir development was also responsible for the development of fracture permeability and creation of hydrocarbon and reduced sulfur chemical traps in the cover rocks. Furthermore, peak oil generation occurred in the Miocene and Pliocene (Belayouni et al. 1992) during accelerated burial in parallel with the Alpine orogenic events. About 50 km south of the Bou Jaber mine, the main oil fields produce hydrocarbons from the Aptian limestones reservoir, similar to that hosting the Bou Jaber ores.Perhaps the reason for mineralization in some diapirs and not others could be the "quality" of the chemical traps or the involvement of some "special" steeply dipping deep-seated faults (perhaps the NW-SE faults that cut the NE-SW trend of the diapirs). The proposed migration of the deep-seated brines during the Alpine orogeny, related to the effects of Alpine collision, provided uplift of the basin and over pressured fluids from thrust stacking and burial maturation of organic matter.

The previous discussion on deposition of the Zn-Pb rich ores proposed a fluid-mixing precipitation model that applies to many sediment hosted Zn-Pb ores (e.g., Cooke et al, 2000; Leach et al, 2005). However, an enigmatic question is how do the barite and fluorite events connect or not to the Zn-Pb ores at Bou Jaber? Although Zn-Pb, barite and fluorite ores do occur together in some ore zones in Bou Jaber, this association is inconsistent within the deposit as well as in the region (few mineralized diapirs contain all three mineral assemblages).The three mineral assemblages are clearly geochemically and paragenetically distinct but yet they were controlled by the same diapiric structures related to the Alpine orogeny in the Miocene-Pliocene times. As pointed out previously, the geochemical constraints on a hot basinal brine in a carbonate platform limits the ability of a single fluid to transport ore-grade amounts of Zn, Pb, Ba and F. Consequently, we suggest that an evolving tectonic and structural regime during the Alpine orogeny, resulted in the ascent of fluids from distinctly different fluid reservoirs. Zn-Pb rich ores formed by the mixing of an oxidized Zn-Pb brine into a hydrocarbon reduces sulphur gas reservoir, barite formed by the mixing of a Ba-rich fluid with sulphate-rich fluids and meteoric water in the diapiric zone and fluorite was deposited in the diapiric zone from a Na-rich brine by cooling, dilution, pH change in the diapiric zone.

Exploration Implications

Given the abundance of salt diapirs in the region, an obvious question is why do only a few have significant Zn-Pb mineralization? A likely factor that determines whether mineralization will occur in a diapir zone is the quality and size of the hydrocarbon and reduced sulfur reservoir. The essential role of a salt diapir in the mineralization process is the formation of a structural trap or reservoir around the diapir for hydrocarbon and reduced sulfur gases. The hydrocarbon and reduced sulfur-rich reservoir in the peridiapiric zone provides a

chemical trap for ascending metalliferous brines. Factors that influence the quality of the trap are the abundance of gypsum/anhydrite in the mother salt, the size of the structural trap and the permeability and porosity of the reservoir. The traps at Bou Jaber may have involved the diapir itself or the Albian shale as the reservoir "seal" in the peridiapiric zone. Additionally, contacts between the Triassic evaporites and the Cretaceous shale (on both sides of the evaporite diapir) are potentially important traps that have not been recognized in the past.

The ores at Bou Jaber and other large tonnage deposits in the diapir belt are located in -or adjacent to- organic-rich peridiapiric rocks along the south-eastern flank of northwest dipping diapirs. Mineralization is especially common at the NE and SW extremities of the diapir. The locations of the ores appear to coincide with the possible intersections of the SW-NE deep basement faults and NW-trending faults limiting Miocene-Pliocene NW-trending grabens were controlled by the interaction of NW-SE to EW trending, deep seated and steeply dipping faults that may have been the vertical pathway for ascending metalliferous brines that precipitated ores in the peridiapiric zone. Therefore, the connectivity of faults in the basement with the upper diapiric zones must have been essential. Lacking the connectivity, a salt diapiric zone would remain sterile in sulfide mineralization.

A significant conclusion of the study provides evidence that decouples the mineral assemblages (Zn-Pb, fluorite and barite) into separate and genetically unrelated mineralization events. Consequently, the presence of barite or fluorite mineralization in any diapiric zone does not necessarily suggest the presence of Zn-Pb rich ores.

Conclusions

This paper provides new insights into the ore-forming environment, sources of the ore components and geological controls that produced the sphalerite, galena, barite and fluorite ores of the Bou Jaber deposit. In contrast to previous authors, we show that the Zn-Pb, barite and fluorite mineral assemblages were produced by at least three separate and possibly unrelated mineralization events. However, it is unclear how these separate events are related to specific tectonic events and structural controls.

The exact age/s of the ores are uncertain. Field relations are consistent with mineral deposition during the Miocene Alpine Orogeny from multiple hydrothermal events: (1) Zn-Pb sulfides formed the mixing of two fluids: one fluid metal-rich but reduced sulfur-poor and a second fluid containing reduced sulfur; (2) the fluorite precipitated during from a more dilute fluid with higher temperatures; (3) barite precipitation involved the influx of a meteoric water component that mixed with a barium-rich fluid.

Although the Bou Jaber ores are hosted in peridiapiric rocks, the fundamental genetic characteristics of the ore deposit are remarkably similar to those for the MVT family. There are no obvious connections to

igneous events. The presence of abundant barite and fluorite with the Zn-Pb ores is unusual for a MVT deposit; however they overprinted a distinct and older Zn-Pb event. Therefore, the ores of Bou Jaber can clearly be classified as "MVT" or as a "MVT sub-type" or as Salt Diapir-related Zn-Pb ores

The deposition of Zn-Pb ores was determined by the presence of a hydrocarbon-reduced sulphur reservoir about the salt diapir. Undoubtedly, the quality of the sulphur trap played a major role in the endowment of Zn-Pb of the deposit. Factors that influence the quality of the trap are the abundance of gypsum/anhydrite in the mother salt, the size of the structural trap and the permeability and porosity of the hydrocarbon-reduced sulphur reservoir.

The Zn-Pb ores at Bou Jaber resulted from the mixing of metalliferous sedimentary brine with reduced hydrocarbon-reduced sulfur reservoir in the peridiapiric environment. Consequently, a deep-seated (basement?) fluid component must have an efficient fluid pathway to ascend into the chemical sink in the peridiapiric zone. Therefore, the connectivity of faults in the basement with the upper diapiric zones was essential.

The studies presented here provide new insights into the genesis of the Bou Jaber Pb-Zn-Ba-F ore deposit and suggest that new research will be needed to improve our understanding of MVT ores in diapiric environments both in Tunisia and globally. In view of the giant diapiric ores of Jinding China, future discoveries of large resources of diapir-related ores in North Africa and globally require an increased focus on exploration in the peridiapiric environment.

Acknowledgements – We wish to thank Fethi M'Barek, director of the Bou Jaber mine, for his assistance to made possible underground ore examinations and sampling. We wish also to thank Cyndi Kester, for assistance during the C, O and S isotopes analysis. The authors thank the following individuals for helpful discussions on the geology and halokinesis of the Bou Jaber diapir: Habib Belayouni, Saïd Tlig; Ali Zaier from the University of Tunis El Manar; Ahmed Brahem from the Office National des Mines Tunisia and Larbi Raddad from the College of the City University of New York. Discussions with Pr. Habib Belayounion the organic matter and mineralisation relationships were strongly helpful. Review by Karen Kelley, from the USGS Denver, significantly improved the manuscript. Financial aid was provided to Salah Bouhlel by a research grant from the C.I.E.S/U.S.A, Fulbright program.

References

Akrour H, Aoudjehane M, Othmanine A, Thibieoz J, Touahri B (1991) Gites et indices de fluorine de l'Algérie du Nord : Inventaire et réflexion. Bull de l'Office National de Géologie Alger 2(1):11–28

Allan MM, Yardley BWD, Forbes LJ, Shmulovich KI, Banks DA, Shepherd TJ (2005) Validation of LA-ICP-MS fluid inclusion analysis with synthetic fluid inclusions. Am Mineral 90:1767–1775

Amouri M (1989) Les minéralisations Pb-Zn-Ba-F liées aux faciès carbonatés aptiens dans l'Atlas Tunisien Central. Géologie Méditerranéenne XVI 2-3:85–199, Marseille

Banks DA, Giuliani G, Yardley BWD, Cheilletz A (2000) Emerald mineralization in Colombia: fluid chemistry and the role of brine mixing. Miner Deposita 35:699–713

Belayouni H, Chandoul H, Mrad R (1992) Oil seep and associated phenomena in northern Tunisia. Field Trip guidebook, III^{ème} Journées de Géologie Tunisienne Appliquées à la Recherche des hydrocarbures ETAP Tunis

Belayouni H, Brunelli D, Clocchiatti R, Di Staso A, El Hassani I, Guerrera F, Kassaa S, Laridhi-Ouazaa N, Martín M, Serrano F, Tramontana M (2010) La Galite Archipelago (Tunisia, North Africa): Stratigraphic and petrographic revision and insights for geodynamic evolution of the Maghrebian Chain. J African Earth Sciences 56 (1):15–28.

Béjaoui J, Bouhlel S, Cardellach E, Canals A, Perona J, Piqué A (2013) Mineralization and fluid inclusion studies of the Aptian carbonate-hosted Pb-Zn-Ba ore deposits at Jbel Hamra, Central Tunisia. J Geoch Explor 128:136–146

Bellon H (1976) Séries magmatiques néogènes et quaternaires du pourtour de la Méditerranée occidentale, comparées dans leur cadre géochronologique; implications géodynamiques. Thèse Etat Orsay

Ben Ayed N (1986). Évolution tectonique de l'avant- pays de la chaîne alpine de Tunisie du début du Mésozoïque à l'Actuel. Thesis University Paris Sud, Paris.

Bodnar RJ (1993) Revised equation and table for determining the freezing-point depression of H2O-NaCl solutions. Geochim Cosmochim Acta 57:683–684

Boltenhagen C (1985) Paléogéographie du crétacé moyen de la Tunisie centrale. 1er Congr. Nat. Sci. Terre 1:97–114

Bolze J (1954) Ascension et percée de diapirs au Crétacé moyen dans les monts de Téborsouk. C R somm Soc Géol France 7:139–141

Bouabdellah M, Brown AC, Sangster DF (1996) Mechanisms of formation of internal sediments at the Beddiane lead-zinc deposit, Toussit mining district, northeastern Morocco. Econ Geol Spec Publ 4:356–363

Bouabdellah M, Castorina F, Bodnar RJ ,Banks D, Jébrak M, Prochaska W, Lowry D, Klügel A, Hoemle M (2013) Petroleum Migration, Fluid Mixing, and Halokinesis as the Main Ore-Forming Processes at the Peridiapiric Jbel Tirremi Fluorite-Barite Hydrothermal Deposit Northeastern Morocco. Econ Geol 109:1223–1256

Bouhlel S (1982) Distribution du baryum et du strontium dans la province fluorée tunisienne; application aux gîtes de Hammam Jédidi et Hammam Zriba-Jebel Guebli. Thesis University of Toulouse III

Bouhlel S (1985) Composition chimique, fréquence des minéraux de la série barytine-célestite dans les gisements de fluorine de Hammam Jédidi et Hammam Zriba-Jebel Guebli (Tunisie Nord-Orientale). Bull Minéral 108: 403–420

Bouhlel S (1987) Mineralized carbonates in fluorite and Pb-Zn ore deposits: Jurassic and Upper Cretaceous of northern Tunisia. In: Excursion Guidebook I.A.S. 8th Regional Meeting of sedimentology pp 1-44

Bouhlel S, Fortuné JP, Guilhaumou N, Touray JC (1988) Les minéralisations stratiformes à F-Ba de Hammam Zriba, Jebel Guebli (Tunisie Nord Orientale): l'apport des études d'inclusions fluides à la modélisation génétique. Miner Deposita 23:166–173

Bouhlel S (1993) Gîtologie, minéralogie et essai modélisation des minéralisations à F-Ba-Sr-Pb-Zn-(S°) associées aux carbonates (jurassiques et crétacés) et aux diapirs triasiques : gisements de Stah-Kohol, Zriba, Guebli, Bou Jaber et Fedj el Adoum (Tunisie septentrionale). Thesis University of Tunis El Manar Tunisia.

Bouhlel S (2005) Carbonate-hosted Mississippi Valley-type Pb-Zn deposits in Tunisia (eastern Atlassic Foreland belt). In Zhao C and Guo B (eds) Mineral deposits research—Meeting the global challenge: China Land Publishing House, Proceedings of the Eighth Biennial SGA Meeting (Beijin, China) 3:19–22

Bouhlel S, Johnson CA, Leach DL (2007) The peridiapiric-type Pb-Zn deposit at Fedj el Adoum, Tunisia: geology, petrography, and stable isotopes. In Andrew CJ et al. (eds) Proc Ninth Biennial SGA Meeting (Dublin, Ireland) 1:323–326

Bouhlel S, Leach DL, Johnson CA, Lehmann B (2009) Ore Textures and Isotope Signatures of the Peridiapiric Carbonate-Hosted Pb-Zn deposit of Bou Grine, Tunisia. In Smart Science for Exploration and Mining P. J. Williams et al. (eds) Proceedings of the Tenth Biennial SGA Meeting (Townsville, Australia) 1:409–411

Bouhlel S, Garnit H, Béjaoui J, Skaggs S (2013) Lead isotopes signatures of the MVT lead-zinc (±F) deposits across Central-North Tunisia: Evidence for the heterogeneity in uranium component of the underlying source rocks. In: Mineral deposit research for high-tech world Erik Jonsson et al. (eds) Proceedings of the 12th Biennial SGA Meeting (Uppsala, Sweden) 2:612–615

Bouzenoune A, Lécolle P (1997) Petrographic and geochemical arguments for hydrothermal formation of the Ouenza siderite deposit (NE Algeria) Miner Deposita 32:189–196

Braham A, Hatira N, Hammami M, Kadri A, Arfaoui M, Chihi L, Mansouri A, Souid R (2002) Le diapir de Bou Jaber Tunise Centre Ouest) Précisions biostratigraphiques et conséqunces structurales. Serv Géol Tunisie 69:93–103

Burke WH, Denison RE, Hetherington EA, Keopnick RB, Nelson HF, Otto JB (1982) Variation of seawater $^{87}8r/^{86}Sr$ throughout Phanerozoic time, Geology 10:516–519

Burollet PF (1956) Contribution à l'étude stratigraphique de la Tunisie centrale. Ann Min Géol (Tunis) No.18

Calvez JY, Orgeval JJ, Marcoux E (1986) Etude isotopique du plomb du gisement de Bou Grine (Zone des dômes, Tunisie) et comparaison avec quelques données de la province tunisienne. BRGM Sci Tech 121–123

Charef A, Sheppard SMF (1987) Pb-Zn mineralization associated with diapirism: fluid inclusion and stable isotope (H, C, O) evidence for the origin and evolution of the fluids at Fedj-el-Adoum, Tunisia.Chem Geol 61:113–134

1001 Chihi L (1995) Les fossés néogènes à quaternaires de la Tunisie et de la mer pélagienne: leur étude structurale et
1002 leur signification dans le cadre géodynamique de la méditerranée centrale. Thesis University of Tunis El Manar
1003 Tunisia
1004 Claypool GE, Molsen WT, Kaplan IR, Sakai M, Zak I (1980) The age of curves of sulfur and oxygen isotopes in
1005 marine sulfate and their mutual interpretation. Chem Geol 28:199–260
1006 Cohen, C.R., Schamel, S. and Boyd-Kaygi, P. (1980) Neogene deformation in Northern Tunisia: origin of the
1007 Eastern Atlas by microplate-continental margin collision. Geol Soc Am Bull 91:225–237
1008 Cooke DR, Bull SW, Large RR, Peter J. McGoldrick PJ (2000) The Importance of Oxidized Brines for the
1009 Formation of Australian Proterozoic Stratiform Sediment-Hosted Pb-Zn (Sedex) Deposits. Econ Geol 95:1–18
1010 Decrée S (2008) Caractérisation géochimique et isotopique dans un système d'altération complexe du protolithe
1011 magmatique à la minéralisation fer-plomb-zinc : le cas de la mine de Sidi Driss. Thesis University libre of
1012 Bruxelle
1013 Decrée S, Marignac C, De Putter T, Deloule E, Liégeois JP, Demaiffe D (2008) Pb-Zn mineralization in a Miocene
1014 regional extensional context: The case of the Sidi Driss and the Douahria ore deposits (Nefza mining district,
1015 northern Tunisia). Ore Geology Reviews 34:285–303
1016 Dubourdieu G (1956) Étude géologique de la région de l'Ouenza (confins algéro-tunisiens). Serv Carte Géol
1017 Algérie Alger No. 10
1018 Frank MH, Lohmann KC (1986) Textural and chemical alteration of dolomite: Interaction of mineralizing fluids and
1019 host rock in a Mississippi Valley-type deposit, Bonneterre Formation, Viburnum Trend. In: Hagni RD (eds)
1020 Process mineralogy VI: Warrendale PA Metallurgical Society 103–116
1021 Fuchs Y (1973) Sur les relations entre émersion et concentration métallifére (quelques exemples tunisiens). In:
1022 Livre Jubilaire Solignac. Ann Mines Géol Tunis 26:479–509
1023 Garnit H, Bouhlel S, Barca D, Craig AJ, Chtara C (2012) Phosphorite-hosted zinc and lead mineralization in the
1024 Sekarna deposit (Central Tunisia). Miner Deposita 47:546–562
1025 Gharbi M, Ben Ayed N, Ben Said EA (1985) Essai d'interprétation tectonique du champ filonien de Bou Jaber
1026 (Atlas Tunisien Central). Acte 1er Congr Sc Terre Tunis 1:393–403
1027 Giesemann A, Jager HJ, Norman AL, Krouse HR, Brand WA (1994) On-line sulfur determination using an
1028 elemental analyser coupled to a mass spectrometer. Analytical Chemistry 66:2816–2819
1029 Grandia F, Canals À, Cardellach E, Banks DA and Perona J (2003) Origin of Ore-Forming Brines in Sediment-
1030 Hosted Zn-Pb Deposits of the Basque-Cantabrian Basin, Northern Spain. Econ Geol 98:1397–1411
1031 Goldstein RH, Reynolds TJ (1994) Systematics of fluid inclusions in diagenetic minerals. SEPM Short Course
1032 31:1–199
1033 Guilhaumou N, Szydlowski N, Pradier B (1990) Characterization of hydrocarbon fluid inclusions by infra-red and
1034 fluorescence microspectrometry. Min Mag 54:311–324
1035 Guillong M, Meir DL, Allan MM, Heinrich CA, Yardley BWD (2008). SILLS: A Matlab based program for the
1036 reduction of Laser Ablation ICP-MS data of homogeneous materials and inclusions. Miner Assoc Canada Short
1037 Course 40:328–333

Guirand R, Maurin JC (1991) Le rifting en Afrique au Crétacé inférieur: synthèse structurale, mise en évidence de deux étapes dans la génèse des bassins, relation avec les ouvertures océaniques peri-africaines. Bull Soc Geol Fr 162(5):811–823

Hanna M. A., and Wolf, A. (1934) Texas and Louisiana salt dome cap rock minerals: Bull Am Ass Petr Geol 3: 212–225

Jrad L, Perthuisot V (1995) Diapirisme, orogenèse et mineralization Pb-Zn en Afrique du Nord: exemple des gisements du J. Ajred et du J. Hamra en Tunisie centrale. C R Acad Sci Paris 321:721–728

Juteau M, Michard A, Albared F (1986) The Pb-Sr-Nd isotope geochemistry of some recent circum-Mediterranean granites. Contr Miner Petro 92:331–340

Kampschulte A, Srauss H (2004) The sulfur isotopic evolution of Phanerozoic seawater based on the analysis of structurally substituted sulfate in carbonates. Chem Geol 204:255–286

Kendrick MA, Burgess R, Leach D and Patrick RAD (2002) Hydrothermal fluid origins in Mississippi Valley-type ore deposits: Combined noble gas (He, Ar, Kr) and halogen (Cl, Br, I) analysis of fluid inclusions from the Illinois-Kentucky Fluorspar District, Viburnum Trend, and the Tri-State Districts, Midcontinent United States. Econ Geol 97:453–469

Koepenick RB, Burke WH, Denison RE, Hetherington EA, Nelson HF, Otto JB, Waite LE (1985) Construction of the seawater $^{87}Sr/^{86}Sr$ curve for the Cenozoic and Cretaceous: supporting data. Chem Geol 58(1-2):55–81

Kyle JR, and Price PK (1986) Metallic sulphide mineralization in salt-dome cap rocks, Gulf Coast, U.S.A. Transactions Institution Mining Metallurgy Section B 95:B6-B16

Kyle JR, and Posey HH (1991) Halokinesis, cap rock development and salt dome mineral resources. In: Melvin JL (eds) Evaporites Petroleum and Mineral Resources: Developments in Sedimentology 50:413-474

Land LS (1980) The isotopic chemistry and trace element geochemistry of dolomite: the state of the art. SEPM 28:87–110

Lange S, Chaudhuri S, Clauer N (1983) Strontium isotopic evidence for the origin of barites and sulfides from the Mississippi Valley-type ore deposits in southeast Missouri. Econ Geol 78(6):1255–1261

Laridhi-Ouazaa, N., 1994. Etude mineralogique et geochimique des episodes magmatiques mesozoiques et miocenes de la Tunisie. Thesis University of Tunis El Manar, Tunisia

Leach DL and Sangster DF (1993) Mississippi Valley-type lead-zinc deposits. In: Kirkham RV, Sinclair WD, Thorp RI, Duke JM (eds) Mineral Deposit Modelling Geol Ass Canada Spec Paper 40: 289–314

Leach DL, Sangster DF, Kelly KD, Large RR, Carven G, Allen CR, Gutzmen J, Walters S (2005) Sediment- Hosted Lead-Zinc Deposits: a Global Perspective. In: Hedenquist JW, Thompson JFH, Goldfarb RJ, Richards JP (eds) Econ Geol 100th anniversary volume, pp 561–607

Leach DL; Macquar JC, Langneau V; Leventhal J; Emsbo P; Premo W (2006) Precipitation of lead–zinc ores in the Mississippi Valley-type deposit at Trèves, Cévennes region of southern France. Geofluids 6:24–44

Leach DL, Song, Yucai, Hou, Zengqian, Yang, Tiannan and Xue, Chuandong (2013)The Giant Jinding Zn-Pb deposit: Ore Formation in an Evaporite Dome, Lanping Basin, Yunan, China. In: Mineral deposit research for

high-tech world Erik Jonsson et al. (eds) Proceedings of the 12th Biennial SGA Meeting (Uppsala, Sweden) 3:1424-1427

Leach DL, Taylor RD, Fey DL, Diehl SF and Saltus RW (2010) A deposit model for Mississippi Valley-Type lead-zinc ores. In: Mineral deposit models for resource assessment. http://www.usgs.gov/ pubprod.

Light MPR, Posey HH, Kyle JR, and Price P E (1987) Model for the origins of geopressured brines, hydrocarbons, cap rocks and metallic mineral deposits: Gulf Coast, U.S.A. In: Lerche L, O'Brien J (eds) Dynamical Geology of Salt and Related Structures, Academic Press, pp. 497–542

Maameri K, Daadouch I (1986) Etude des indices de pétrole en surface dans la Tunisie des avant-nappes. Mémoire de Fin d'Etude Ingénieur, Faculté des Sciences de Tunis, University of Tunis El Manar Tunisia

Macquar JC, Rouvier H, Thibiéroz J (1990) Les minéralisations Zn, Pb, Fe, Ba, F péri-cévenoles: cadre structuro-sédimentaire et distribution spatio-temporelle. Doc BRGM Orléans 183: 143–158

Machel HG, Krouse HR, Sassen R (1995) Products and distinguishing criteria of bacterial and thermochemical sulfate reduction. Applied Geoch 10:373–389

Marie J, Trouve P, Desforges G, Dufaure P (1984) Nouveaux éléments de paléogéographie du Crétacé de Tunisie. Notes Mém TOTALC.F.P No 9

Martinez C, Truillet R (1987) Evolution structurale et paléogeographie de la Tunisie. Mem Soc Geol It 38:35–45

Matlock JF, Misra KC 1993 Sphalerite-bearing detrital 'sand' bodies in Mississippi Valley-type zinc deposits Mascot-Jefferson City district, Tennessee Implications for the age of mineralization. Miner Deposita 28:344–353

McCrea JM (1950) On the isotopic chemistry of carbonates and a paleotemperature scale. J Chem Phys 18:849-857

Mejri F, Burollet PF, Ben Ferjani A (2006), Petroleum Geology of Tunisia, A Renewed Synthesis, Entreprise Tunisienne des activités Pétrolières, Tunis. Memoire No. 22

Mc Limans RK (1975) Systematic fluid inclusion and sulfide isotope studies of the Upper Mississippi Valley Pb-Zn deposits. Econ Geol 70 (7) p. 1324

Mc Limans RK (1977) Geological, fluid inclusion, and stable isotope studies of the Upper Mississippi Valley zinc-lead district, southwest Wisconsin: Ph.D. thesis, Pennsylvania State University

M'Rabet A (1987) Stratigraphie, sédimentation et diagenèse carbonatée des séries du Crétacé inférieur de la Tunisie centrale. Ann Mines Géol Tunis No 30

Nesbitt BE, Muehlenbachs K (1994) Paleohydrogeology of the Canadian Rockies and Origins of Basinal Brines, Pb-Zn Deposits and Dolomitization in the Western Canada Sedimentary Basin. Geology 22:243–246

Orgeval JJ (1994) Peridiapiric metal concentrations: example of the Bou Grine deposit (Tunisian Atlas). In: Fontboté L and Boni M (eds) Sediment-hosted Zn-Pb ores. Society for Geology Applied to Mineral Deposits Spec Publ 10:354–389

Paytan A, Kastner M, Campbell D, Thiemens MH (1998) Sulfur isotopic composition of Cenozoic seawater sulfate. Science 282:1459–1462

Perthuisot V (1978) Dynamique et pétrogenèse des extrusions triasiques en Tunisie septentrionale. Thesis Ecole Normale Sup Paris

1111 Perthuisot V (1981) Diapirism in northern Tunisia. J Struct Geol 3:231–235
1112 Philip H, Andrieux J, Dlala M, Chihi L, Ben Ayed N (1986) Evolution tectonique mio-plio-quaternaire du Fossé de
1113 Kasserine (Tunisie centrale) implications sur l'évolution géodynamique récente de la Tunisie. Bull Soc Géol
1114 France 2(8) No.5-6 : 559–568
1115 Pohl W, Amouri M, Kolli O, Scheffer R, Zachman D (1986) A new genetic model for North African metasomatic
1116 siderite deposits. Miner Deposita 21:228-233
1117 Plumlee GS, Leach DL, Hofstra AH, Landis GP, Rowan EL, Viets JG (1994) Chemical reaction path modeling of
1118 ore deposition in Mississippi Valley-type Pb-Zn deposits of the Ozark region, US Midcontinent. Econ Geol
1119 89:1361–1383
1120 Posey HH and Kyle JR (1988) Fluid-rock interactions in the salt dome environment: an introduction and review.
1121 Chem Geol 74:1–24
1122 Posey HH, Kyle JR, Agee WN (1994) Relations between diapiric salt structures and metal concentrations, Gulf
1123 Coast sedimentary basin, Southern North America. In: Fontboté L and Boni M (eds) Sediment hosted Zn-Pb
1124 ores. Society for Geology Applied to Mineral Deposits Spec Publ 10:140–164
1125 Price PE, Kyle JR (1983) Metallic sulphide deposits in Gulf Coast salt-dome caprocks. Gulf Coast
1126 Assoc Geol Soc Trans 33:189-193
1127 Roedder E (1963) Studies of fluid inclusions, II: Freezing data and their interpretation. Econ Geol 58:167–211
1128 Roedder E (1984) Fluid inclusions. Reviews in mineralogy Am Mineral Soc No12
1129 Rouvier H (1977) Géologie de l'Extrême-Nord tunisien: tectonique et paléogéographie superposées à l'extrémité de
1130 la chaîne nord-maghrébine. Ann Mines Géol Tunis No 29
1131 Rouvier R, Perthuisot V, Mansouri A (1985) Pb-Zn Deposits and salt bearing diapirs in Southern Europe and North
1132 Africa. Econ Geol 80:666–687
1133 Saïdi M, Belayouni H (1994). Etude géologique et géochimique des roches mères albo-vraconienne dans le domaine
1134 de la Tunisie centro-septentrional. Proceeding of the 4th Petroleum Exploration Conference 7:91–116 Tunis
1135 Tunisia
1136 Sainfeld P (1956) The lead-zinc-bearing deposits of Tunisia. Econ Geol 51:150–177
1137 Salmi-Laouar S, Laouar R, Boyce AJ, Boutaleb A, Zerdazi A, Arouch YE (2004) Rapports istotopiques du soufre,
1138 de l'oxygène et du carbone dans le massif de Bou Jaber, NE algerien: Origine des mineralizations à Pb-Zn-Ba et
1139 sources des fluides. Serv Géol Algérie 15:3–25
1140 Salmi-Laouar S, Laouar R, Boyce AJ, Boutaleb A, Lamouroux Ch (2007) Premières données isotopiques sur la mer
1141 triasique dans l'Atlas Saharien Oriental (Algérie). Serv Géol Algérie 18:315–323
1142 Sass-Gustkiewics M (1996) Internal sediments as a key to understanding the hydrothermal karst origin of the Upper
1143 Silesia Zn-Pb ore deposits. Econ Geol Spec Publ 4:171-181
1144 Schmidt SC (1999) Re-activation of the Bougrine Mine, Tunisia. 101st Ann Gen Meeting, Can Inst Min Metal
1145 Petro, Techn Progr CD-ROM : Major Canadian Overseas Project Paper 1:1–9
1146 Sheppard SMF, Charef A, Bouhlel S (1996) Diapirs and Zn-Pb mineralizations: A general model based on Tunisian
1147 (N. Africa) and Gulf Coast (U.SA.). Econ Geol Spec Publ 4:230–243

1148 Skaggs S, Norman N, Garrison E, Coleman D, Bouhlel S (2012) Local mining or lead importation in the Roman
1149 province of Africa Proconsularis? Lead isotope analysis of curse tablets from Roman Carthage, Tunisia. J
1150 Archaeol Sci 39 (4):970–983
1151 Soua M (2009) Structural context of the paleogeography of the Cenomanian-Turonian anoxic event in the eastern
1152 Atlas basins of the Maghreb. CR Geosciences 341 (12):1029–1037.
1153 C. R. Acad. Sci. Paris, 316 (II):
1154 Spangenberg J, Fontboté L, Sharp ZD, Hunziker J (1996) CarbonG and oxygen isotope study of hydrothermal
1155 carbonates in the zinc-lead deposits of the San Vicente district, central Peru. Chem Geol 133:289–315
1156 Sverjensky, DA (1986) Genesis of Mississippi Valley-type lead-zinc deposits. Annual Review of Earth and
1157 Planetary Sciences 14:177–199
1158 Turchyn AV, Schrag DP (2004) Oxygen isotope constraints on the sulfur cycle over the past 10 million years.
1159 Science 303: 2004–2007
1160 Turki MM, Delteil J, Truillet R, Yaich C (1988) Les inversions tectoniques de la Tunisie centro-septentrionale. Bull
1161 Soc Géol France (8) IV 3:399–406
1162 Ulrich MR and Bodnar RJ (1988) Systematic stretching of fluid inclusion II. Barite at 1 atmosphere confining
1163 pressure. Econ Geol 83:1037-1046
1164 Veizer J, Compston W (1974) 87Sr/86Sr composition of seawater during Phanerozoic. Geochim Cosmochim Acta
1165 38:1461–1484
1166 Veizer J, Hoefs J (1976) The nature of O-18 /O-16 and C-13 /C-12 secular trends in sedimentary carbonate rocks.
1167 Geochim Cosmochim Acta 40 (11):1387–1395
1168 Vially R, Letouzey J, Bernard F, Haddadi N, Deforges G, Askri H, Boudjema A (1994) Basin inversion along the
1169 North African Margin: the Sahara Atlas (Algeria). In: Roure F (eds) PeriTethyan platforms. Technip, Paris, pp
1170 79–118
1171 Vila JM., Charrière A (1993) Découverte d'Albien calcaire et de Trias resédimenté au Djebel Bou Jaber (partie
1172 ouest, Algérie); corrélations avec les forages et conséquences sur l'organisation du Crétacé inférieur des confins
1173 algéro-tunisiens. CR Acad Sci 316 (2):243–249
1174 Warren JK. (2000) Evaporites, brines and base metals: low-temperature ore emplacement controlled by evaporite
1175 diagenesis. Australian J of Earth Sciences 47:179–208
1176 Yardley BWD (2005) 100th Anniversary Special Paper: Metal concentrations in crustal fluids and their relationship
1177 to ore formation. Econ Geol. 100:613–632
1178 Zartman RE, Doe BR (1981) Plombotectonics-the model. Tectonophysics 75:135–162

Figures

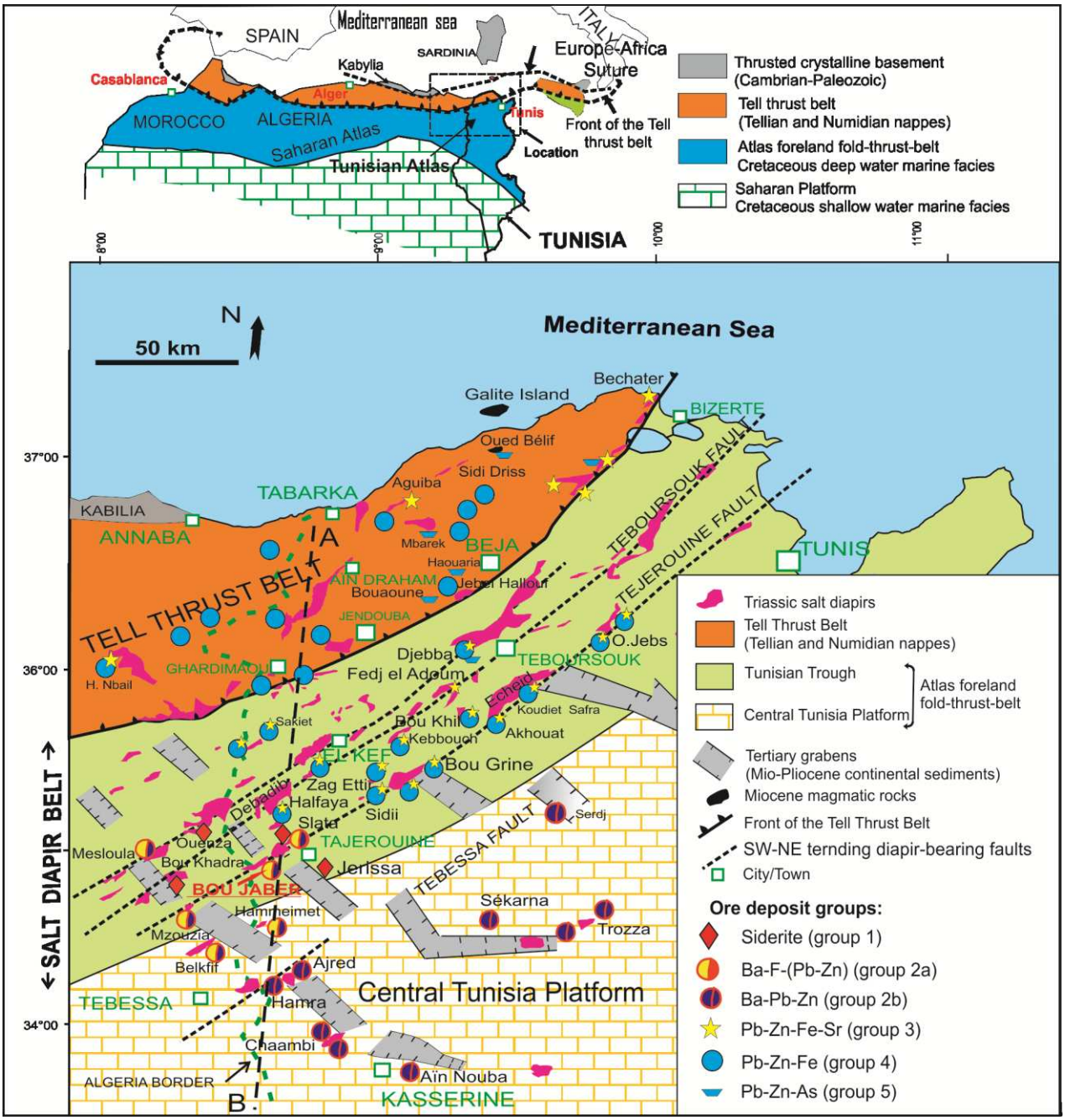

Fig. 1 Simplified structural and paleogeographic map of the Tunisian Salt Diapir Belt and adjacent regions showing the distribution of the Pb-Zn-Fe-Ba-Sr-F deposit groups discussed in text. Most of the ore deposits are spatially connected to Triassic diapirs. Bou Jaber is located at the SW area of the Salt Diapir Belt that corresponded to the SW margin of the Tunisian Trough. A-B line is cross section shown in Figure 2. Regional location is shown on inset map.

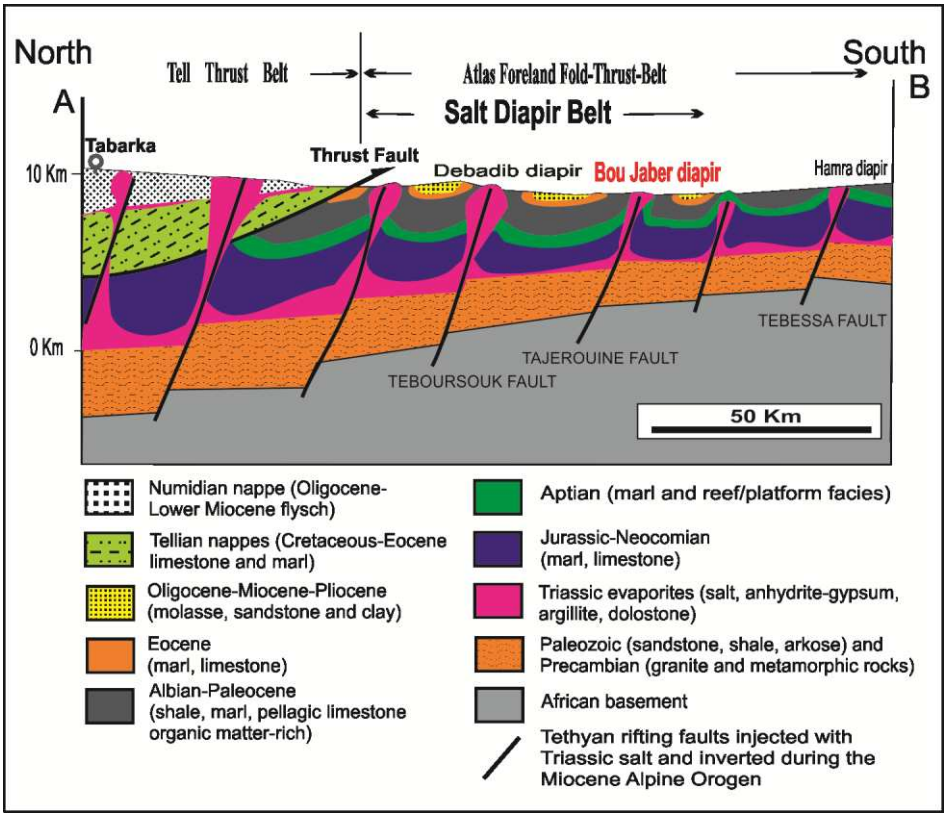

Fig. 2 Present day interpretative N-S structural section of northern-central Tunisia. For location see A-B line in Figure 1.

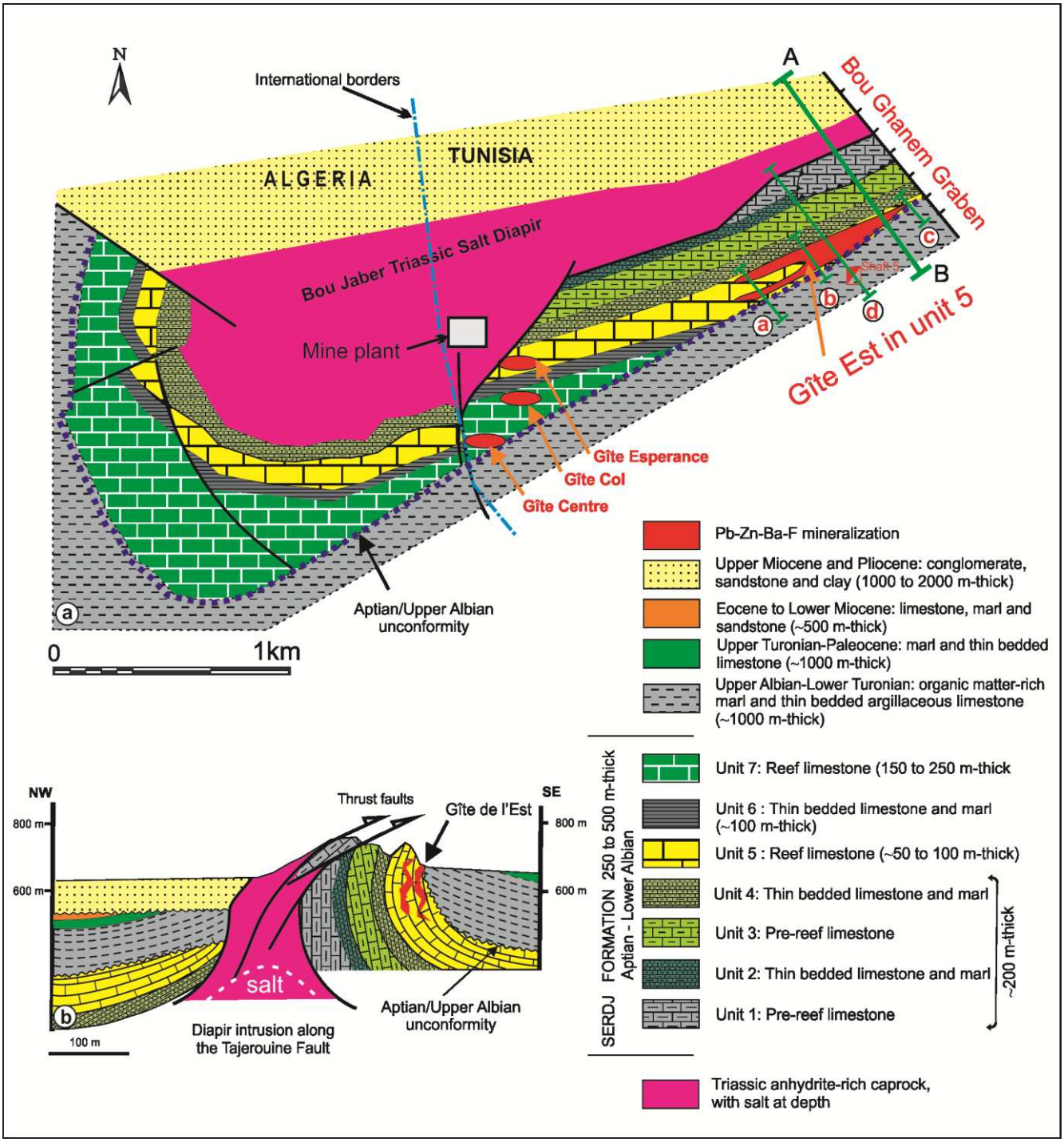

Fig. 3 Geology map of the Bou Jaber Triassic salt diapiric structure showing stratigraphy, principal structural elements and the main F-Ba-Pb-Zn deposits. Circled numbers (1 to 5) correspond to the cross sections in figure 4. **b** Present day NW-SE cross section showing the geometry of the Triassic salt intrusion trough the Tajerouine SW-NE-tending Fault (Cross section is located by the A-B line in figure 3a and the Tajerouine Fault is shown in Figure 1). **c** Interpretative N-S cross section of the Bou Jaber diapiric structure at the end of the Middle Miocene Alpine compression (not to scale)

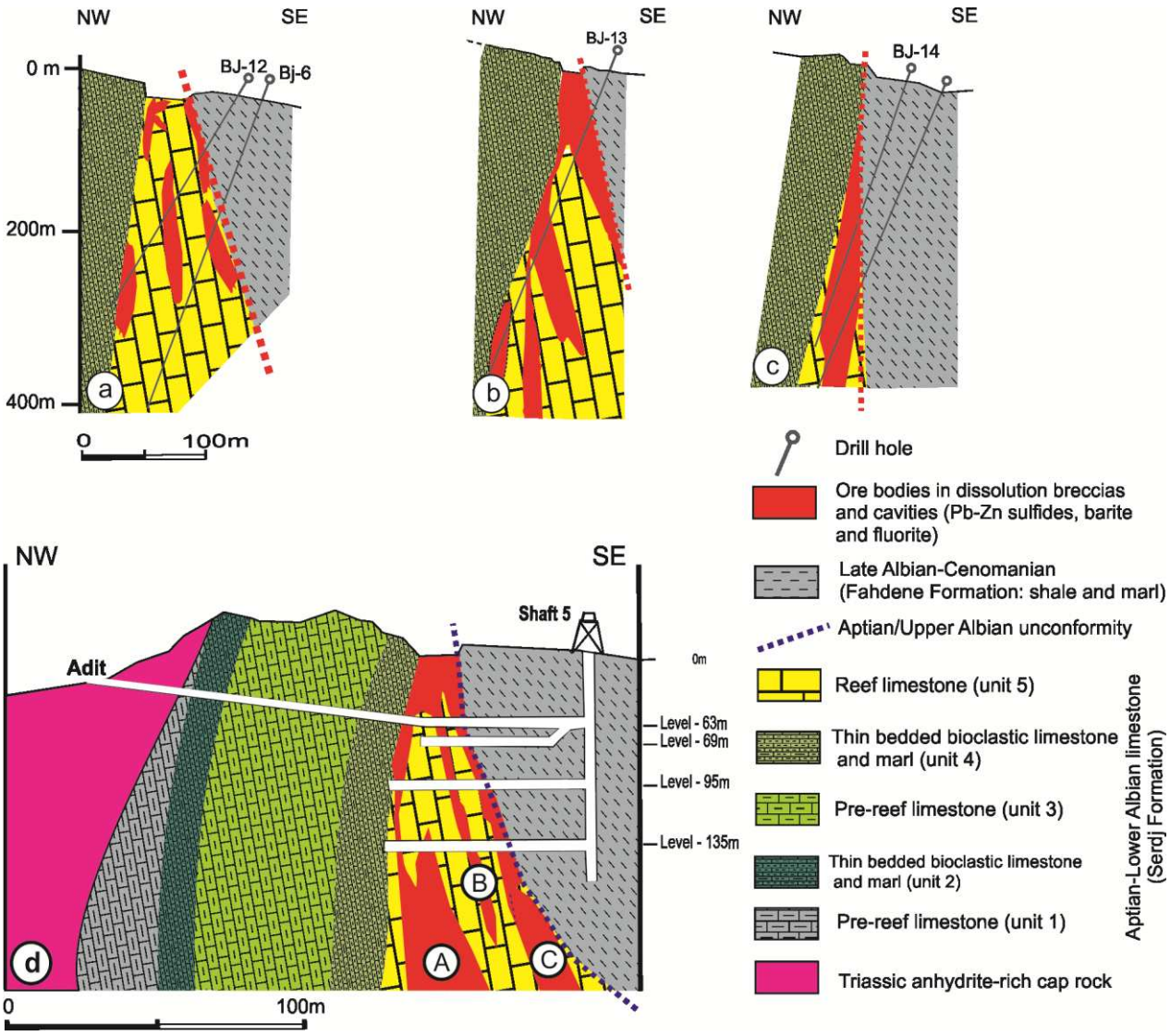

Fig. 4 NW-SE cross sections a, b, c, d of the Bou Jaber "Gîte de l'Est", illustrated on the basis of field mapping in mining open pits, underground working exposures and drill holes. The sections show some of the vertical and lateral variations in volumes of the dissolution-cavities filled with the Pb-Zn-Ba-F ore cross-cutting the Aptian limestone strata. (for location see a, b, c and d lines in Figure 3**b**).

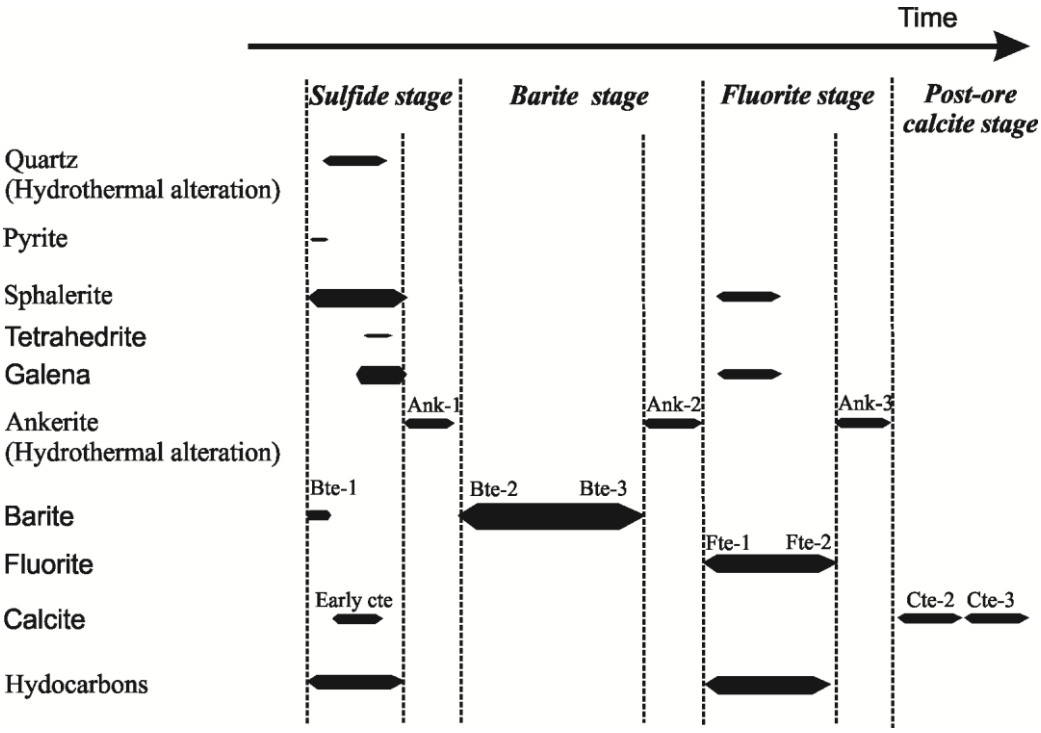

Fig. 5 Schematic paragentic sequence of the ore-, and mineral alteration assemblages in the Bou Jaber (Gîte de l'Est) Pb-Zn-Ba-F deposit. Bars thicknesses reflect abundance of minerals. Hydrocarbons occur as oil seepage in the ore and as oil-bearing fluid inclusions in the sulfide- and fluorite stages.

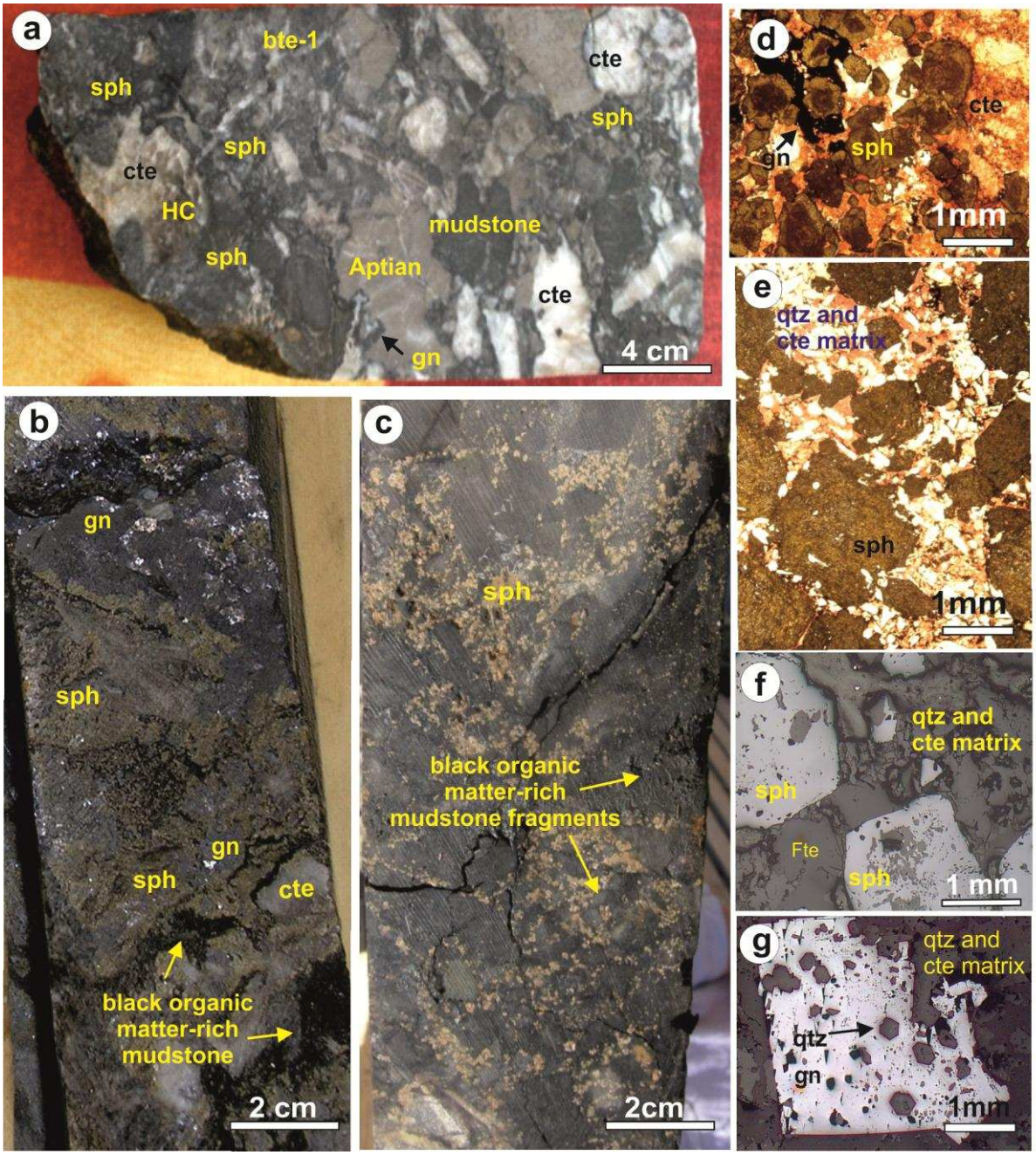

Fig. 6 Drill core samples of zinc-lead rich-ore from dissolution cavities where sphalerite and galena occur by replacement of carbonaceous breccia-matrix. **a** Dissolution breccia sphalerite-rich: Breccia fragments are grey Aptian limestone and black mudstone. The matrix is composed of fine-grained bipyramidal quartz, fine-grained honey sphalerite, galena, minor fine grained barite-1 and calcite. Liquid hydrocarbon (HG) fills cavities in the calcite aggregations. **b** Core sample of high grade massive sphalerite and galena. **c** Core sample of high-grade sphalerite (honey euhedral sphalerite crystals) aggregation in black mudstone breccia calcite-, quartz-, and organic matter-rich. **d** Detail from **c** showing sphalerite crystals cemented by calcite (red-S coloured). **e** detail from **c** showing aggregations of euhedral sphalerite crystals in a quartz- and calcite-rich matrix; quartz is white and calcite is red-S coloured. **f** Euhedral sphalerite in a matrix of calcite and quartz. Calcite is partly replaced by fluorite. **g** Euhedral galena containing bipyramidal quartz relicts of the replaced quartz-, calcite-rich sulfide matrix. **d** and **e** polished sections, transmitted light //; **f** and **g** polished sections, reflected light //.

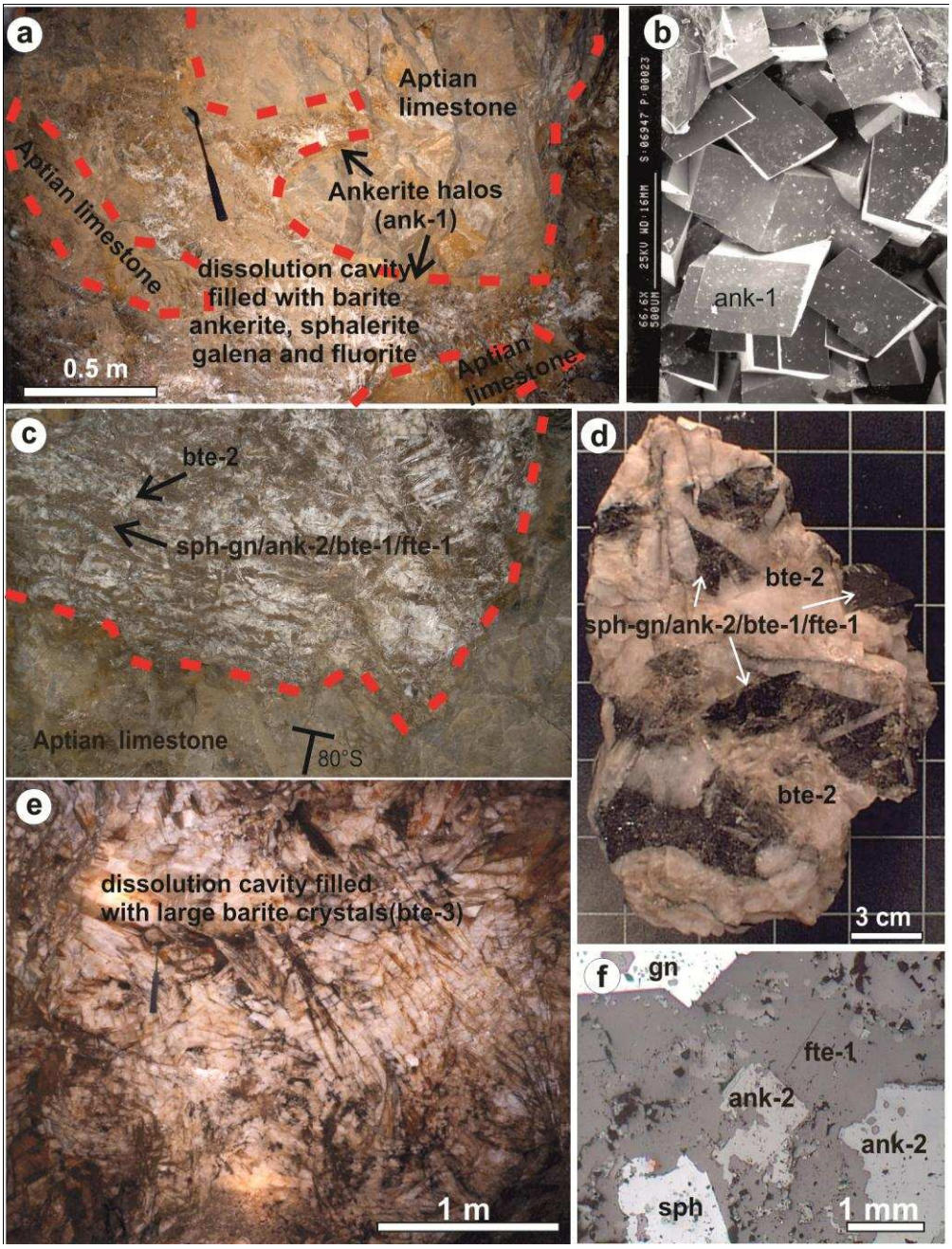

Fig. 7 Hydrothermal dissolution and ankeritization of the Aptian limestones (unit 5) followed by barite deposition in the gîte de l'Est deposit. **a** Hydrothermal dissolution of the Aptian limestones developed large irregular cavities, meter- to plurimeteric-size. An ankerite halo (ank-1), 5- to 50 cm-thick, lines the hydrothermal alteration of the host rock. The infilling material of cavities is composed of ankerite-2 and barite postdating minor sphalerite and galena. b SEM photograph of the euhedral coarse-grained ankerite crystals (ank-1) (sample from the ankerite halo). **c** Banded rich barite ore in dissolution cavity, showing horizontal banding compared to the70°deeping of the Aptian limestones strata. White bands are barite and dark bands are a complex assemblage of ankerite-2, sphalerite, galena and fluorite. **d** sample of banded barite-rich ore. The black matter is composed of ankerite and sulfide where most part of the ankerite is replaced by fluorite (as shown on Fig. 8f). The white bands are composed by tabular cm-size crystals of barite developed often orthogonally to the dark bands. **e** barite zone formed by large barite crystals (central part of the hydrothermal dissolution cavities, underground working at level -95 m). Barite forms tabular crystals 5- to 20 cm-thick and 50- to 100 cm-length (scale is also shown by the hammer). **f** fluorite-1 replacing ankerite matrix of sphalerite and galena crystals, polished section, reflected light //.

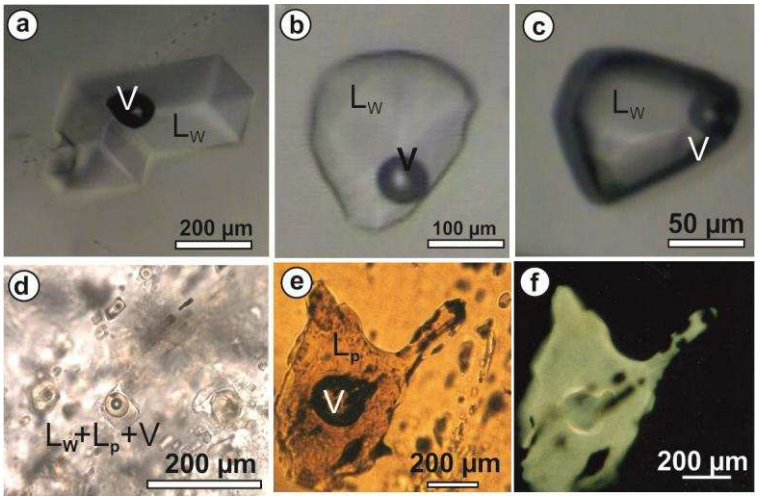

Fig. 8 a and **b** Primary L_w+V fluid inclusions in fluorite. **c** Primary L_w+V fluid inclusions in barite. **d** Primary L_w+L_p+V fluid inclusion in fluorite. **e** Large primary L_p +V fluid inclusion in fluorite. **f** Same as Fig e but under epifluorescence microscope. L_w=water; V= vapour; L_p = Petrolium.

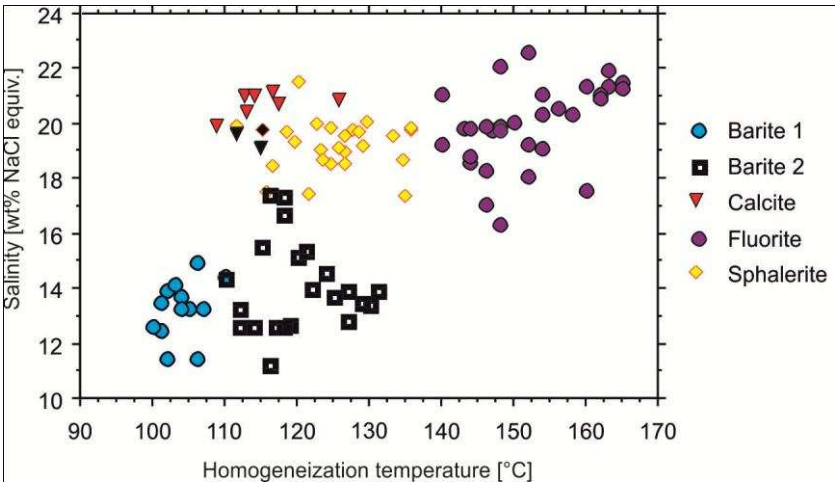

Fig. 9 Plot of Th versus salinity derived from microthermometric studies of fluid inclusions in sphalerite, fluorite, barite and calcite.

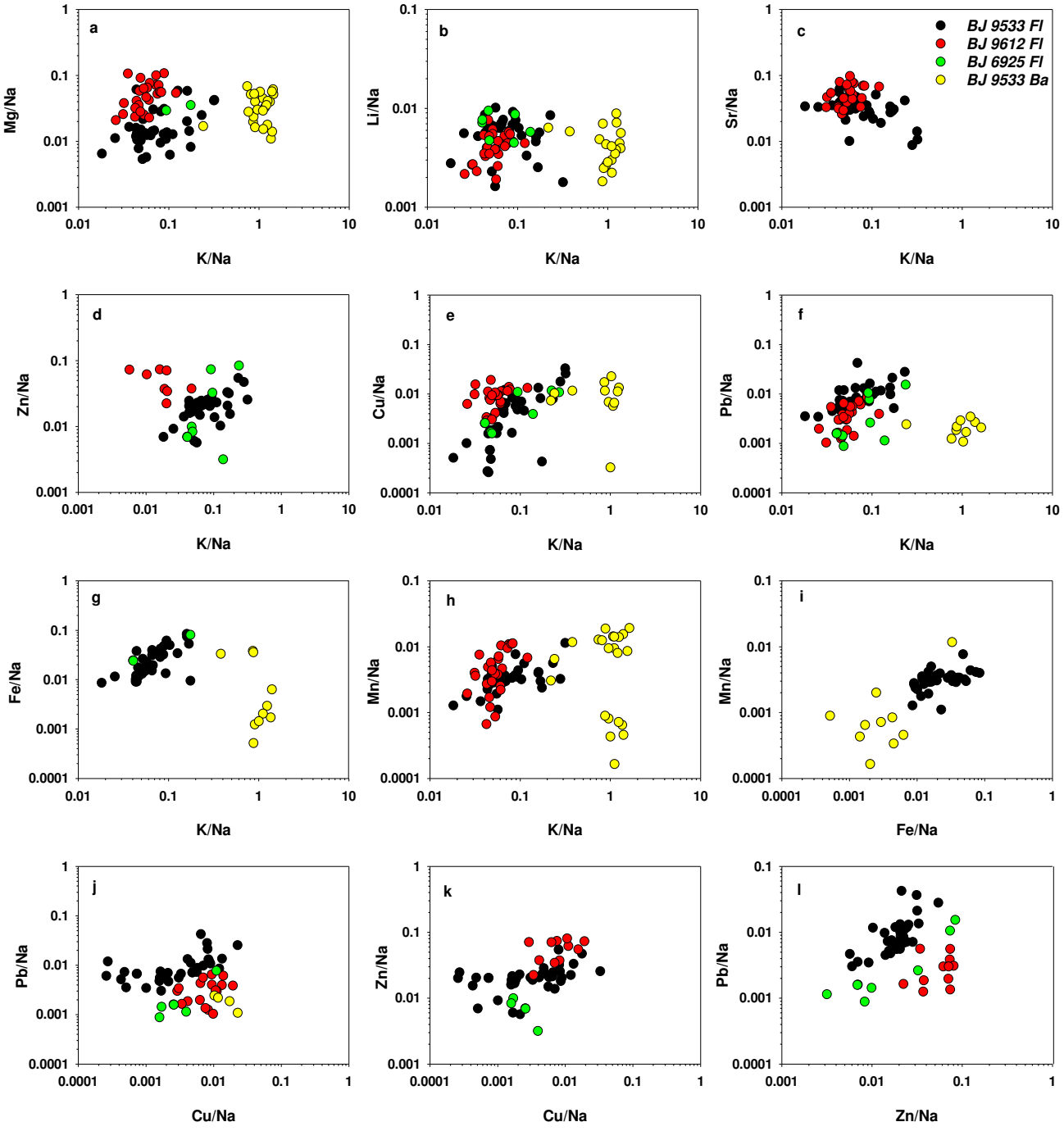

Fig 10 Bi-variate cation/Na weight ratios as determined by LA-ICPMS of fluid inclusions. Inclusions hosted in barite are distinctly different to those in fluorite indicating two fluids involved in mineralization. Analyses from individual samples are tightly clustered and for different fluorite samples largely overlap.

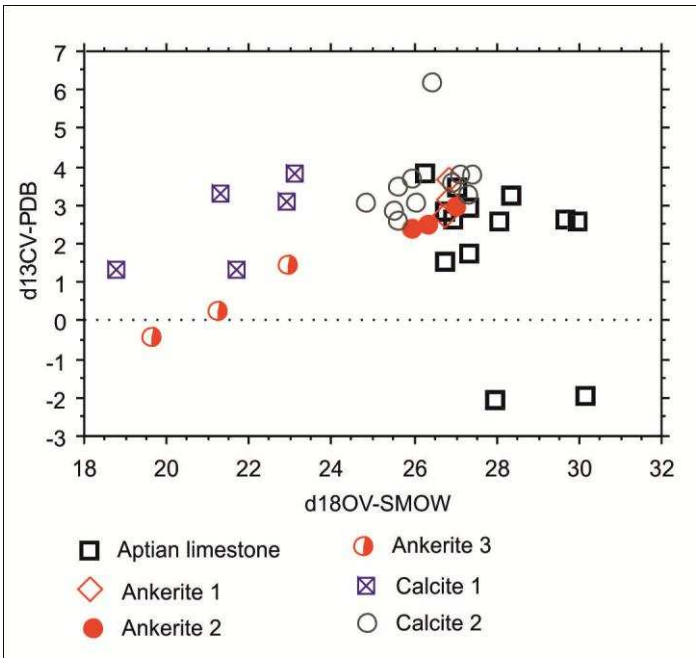

Fig. 11 Diagram $\delta^{13}C$ (PDP) vs $\delta^{18}O$ (SMOW) showing values for ankerite and calcite compared to the Aptian limestone host rock (Bou Jaber deposit).

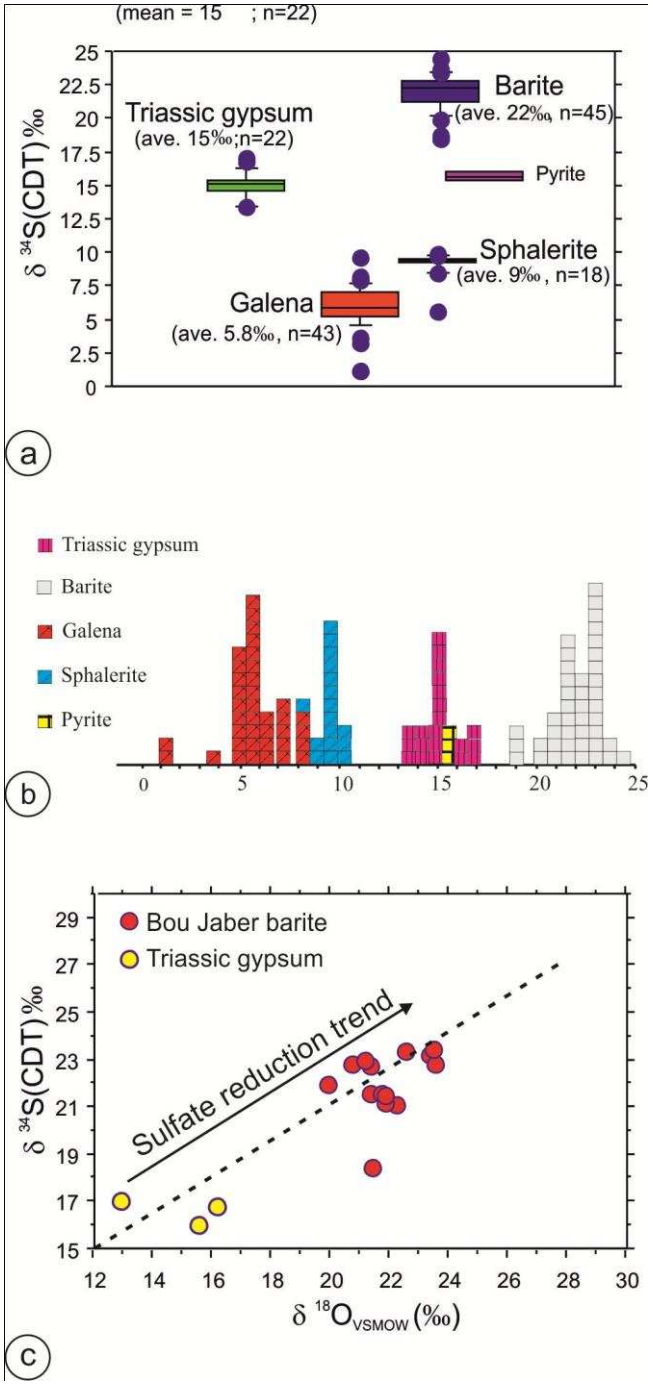

Fig. 12 a Box plot of $\delta^{34}S$ values for sphalerite, galena, pyrite and barite at Bou Jaber, and $\delta^{34}S$ values for regional Triassic gypsum and anhydrite. The sulfur isotope compositions shown are isotopically relatively homogeneous with a composition near 6 ‰ for galena, 9 ‰ for sphalerite, 22 ‰ for barite and 15 ‰ for Triassic gypsum. **b** Histogram distribution of the $\delta^{34}S$ values for sphalerite, galena, pyrite, barite and Triassic gypsum. **c** Plot of $\delta^{18}O$ vs $\delta^{34}S$ of Bou Jaber barites. The $\delta^{18}O$, $\delta^{34}S$ of Triassic anhydrite are also plotted for comparison with barites.

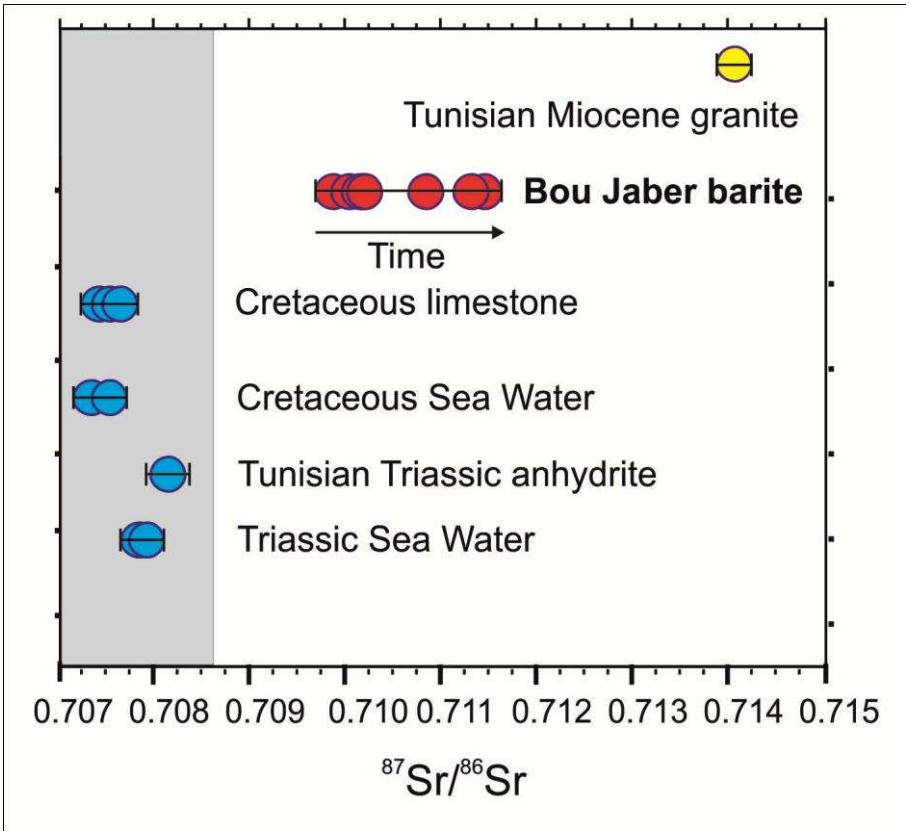

Fig. 13 Strontium isotope ratio diagram comparing Bou Jaber barite ores with Triassic evaporite, Triassic sea water, Cretaceous sea water and with Tunisian Cretaceous sediments ($^{87}Sr/^{86}Sr$ values for Cretaceous sediments are from Orgeval 1994).

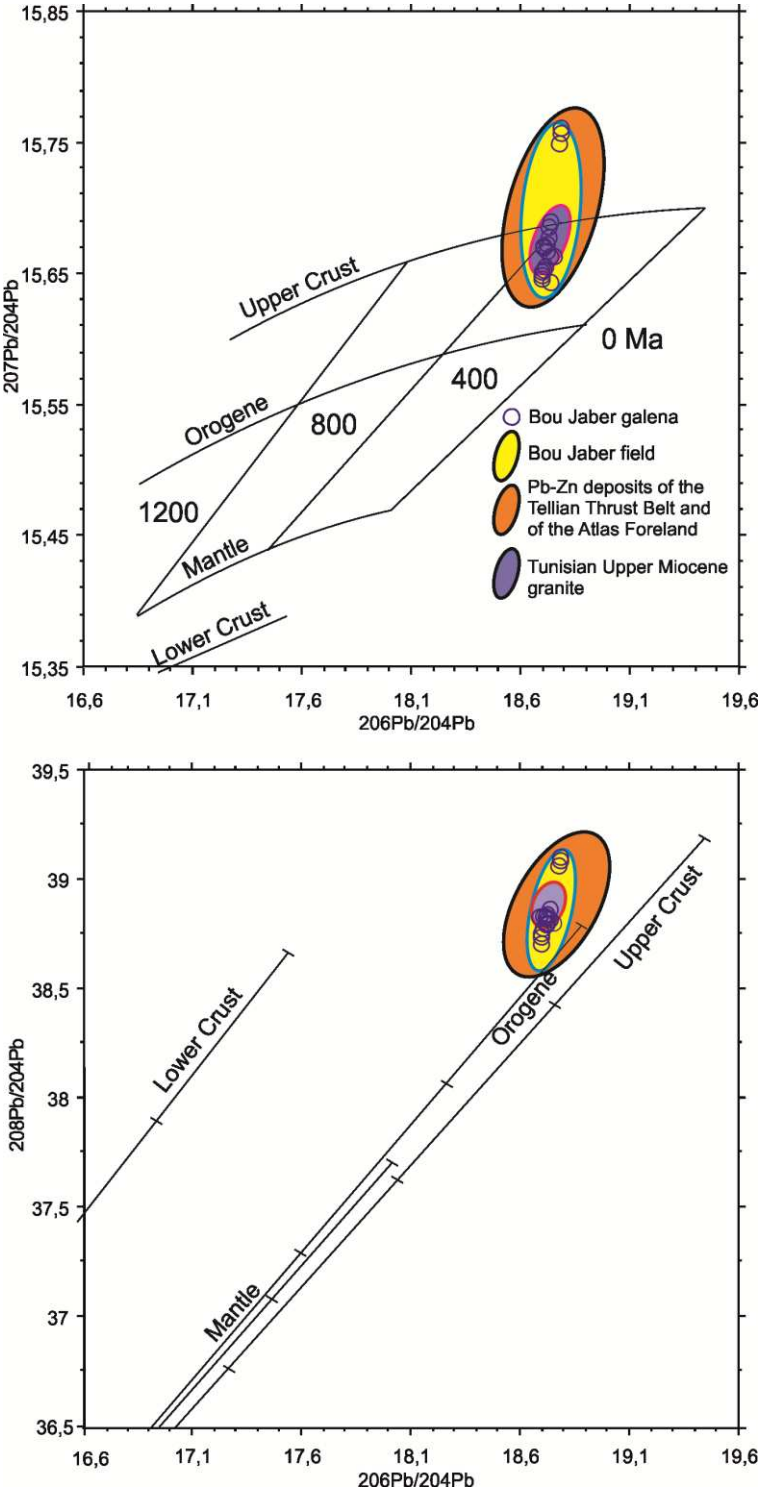

Fig. 14: Lead isotope ratios of galena sample from Bou Jaber Pb-Zn-Ba-F deposit reported in $^{206}Pb/^{204}Pb$ and $^{207}Pb/^{204}Pb$ diagram (uranium derived Pb) (14**a**) and in the $^{208}Pb/^{204}Pb$ and $^{207}Pb/^{204}Pb$ diagram (14**b**). Isotope composition are present-day values are not corrected to age. The upper crust, lower crust, orogen, mantle evolution curves are from Zartman and Doe (1981). Bou Jaber Lead isotope ratios fill in the field of sulfide lead compositions the Tellian thrust belt- and the Tunisian Atlas foreland Pb-Zn deposits (Bouhlel et al. 2013). The Bou Jaber Pb-isotope compositions are also compared to Pb ratios of Tunisian Miocene granite (values are from Juteau et al. 1986 and Decrée 2008.

Table 1: Summary of the microthermometric data derived from the studies of primary fluid inclusions (Lw+V) in sphalerite, barite and fluorite from the Bou Jaber "Gîte de l'Est".

Sample	Mineral	Nbr IF	Te °C	Tm ice °C	Salinity Wt% NaCl equiv.	Th °C
2525C1	Sphal	38	-39 to -32	-16.8 to -14.8	18.5–19.1 (19.2)	112–133 (123)
2525C3	Sphal	34	-40 to-30	-18.7 to -13.4	17.3–21.5 (19.13)	115–136 (125)
6921D	Sphal	28	-40 to -37	-1.7 to -13.6	17.4–19.99 (18.1)	116–136 (128)
	Total		-40 to -30	-18.7 to -13.4	17.2–21.47 (19.1)	112–136 (125)
6925B1	Barite	20	-40 to -39	-11 to -7.8	11.5–15 (13.3)	101–110 (105)
9514BA	Barite	10	-43 to -40	-11.4 to -7.6	11–15 (13.6)	116–124 (120)
95J1	Barite	16	-40 to -38	-10.4 to -8.8	12.6–14.4 (13.2)	110–114 (112)
9533B	Barite	25	-42 to -36	-10 to -8.8	12.6–13.9 (13.4)	100–131 (119)
63WA	Barite	18	-45 to -41	-13.6 to -11.6	15.6–17.4 (16.7)	115–118 (117)
	Total	89	-45 to -36	-13.6 to –7.6	11.2–17.4 (13.9)°	100–131 (114)
8511	Fluorite	34	-42 to -28	-18 to -14	21.5–18.1 (20.1)	140–165 (155)
B8512	Fluorite	60	-42 to -28	-13.8 to 19.4	22–17.6 (19.8)	144–163 (154)
9514AF	Fluorite	52	-32 to -28	-19.6 to -15.8	22.1–19.3 (20.6)	140–163 (150)
95514BF	Fluorite	60	-32 to -28	-20.5 to -15	22.6–18.6 (20.5)	144–162 (153)
9533BF	Fluorite	40	-45 to -40	-18.2 to -12.4	21.1–16.3 (17)	146–154 (145)
	Total	246	-45 to -28	-20.4 to -12.4	16.3 –22.6 (20)	140–165 (152)
63WB	calcite	25	-33.3 to -30	-18.2 to -15.5	20–0.9 (20.8)	113–126 (118)
63WC	calcite	22	-33.3 to -30	-18 to -17	21.1–19.0 (20)	109–117 (113)
	Total	45	-33 to -30	-18.2 to -15.5	19.0–21.1 (20.5)	109–126 (116)

Table 2 LA-ICPMS analyses of individual fluid inclusions in fluorite and barite from levels – 69 m and 95 m,

	BJ9533 Fluorite				BJ6921 Fluorite				BJ6925 Fluorite				BJ9533 Barite			
	Average wt/wt	**StdDev**	**%RSD**	**ppm**	**Average wt/wt**	**StdDev**	**%RSD**	**ppm**	**Average wt/wt**	**StdDev**	**%RSD**	**ppm**	**Average wt/wt**	**StdDev**	**%RSD**	**ppm**
Li	0.00595	0.0020	35.1	**243**	0.00415	0.0013	31.9	**164**	0.00685	0.0019	28.1	**275**	0.00433	0.0020	48.4	**84**
Na	1	0	0	**40914**	1	0	0	**39527**	1	0	0	**40076**	1	0	0	**19334**
Mg	0.01926	0.0143	74.5	**788**	0.05365	0.0259	48.4	**2121**	0.03236	0.0041	12.9	**1297**	0.03417	0.0169	49.5	**661**
K	0.09236	0.0740	80.2	**3779**	0.05780	0.0200	34.7	**2285**	0.13307	0.0842	63.3	**5333**	1.08053	0.3561	33.0	**20891**
Ca	0.5			**20457**	0.5			**19764**	0.5			**20038**	0.5			**9667**
Mn	0.00364	0.0018	50.0	**149**	0.00529	0.0034	64.4	**209**	<0.00595			**<238**	0.00714	0.0065	91.7	**138**
Fe	0.02681	0.0189	70.5	**1097**				**0**	0.04296	0.0325	75.8	**1722**	0.00974	0.0141	144.8	**188**
Cu	0.00624	0.0073	118.3	**255**	0.00935	0.0041	44.7	**370**	0.01115	0.0004	3.9	**447**	0.00745	0.0043	57.8	**144**
Zn	0.02107	0.0092	43.7	**862**	0.05745	0.0196	34.2	**2271**	0.02813	0.0325	115.8	**1127**				**0**
Sr	0.03196	0.0120	37.8	**1308**	0.05385	0.0195	36.3	**2129**				**0**				**0**
Ag	0.00005	0.0000	85.7	**2**	0.00024	0.0002	88.8	**9**	0.00067	0.0006	101.4	**27**	0.00037	0.0003	83.7	**7**
Ba	0.01409	0.0078	56.0	**576**	0.04720	0.0221	47.0	**1866**	0.00690	0.0038	56.2	**276**				**0**
Pb	0.01072	0.0085	79.8	**439**	0.00382	0.0021	55.9	**151**	0.00589	0.0060	103.3	**236**	0.00193	0.0008	41.4	**37**
U	0.00001	0.0000	95.5	**0.3**	0.00013	0.0001	141.8	**5**	0.00043	0.0003	72.9	**17**	0.00005	0.0000	26.1	**1**

Concentrations in fluorite are based on a salinity of 18wt%NaCl, barite salinity of 13wt% NaCl. Ca/Na wt ratio is based on hydrohalite-ice melting temperatures in fluorite and assumed to be the same for inclusions in barite (not possible to measure).

Table 3 Carbon and oxygen isotopes compositions of Aptian limestone host rock, hydrothermal ankerite and calcite from Bou Jaber. Analysis marked with asterisk are from Salmi-Louar 2004; and Salmi-Laouar et al 2007

Samples	Description	$\delta^{13}C$ (‰, PDP)	$\delta^{18}O$ (‰, SMOW)
6928	Aptian limestone	-1.9	30.1
B6930A	Aptian limestone	2.7	29.6
B6929	Aptian limestone	2.6	29.9
9523U5	Aptian limestone	3.3	28.3
9549BC1	Aptian limestone	-2	27.9
69U5C1	Aptian limestone	2.7	26.9
69U5C2	Aptian limestone	3.9	26.2
6929U5	Aptian limestone	2.6	28
BJU5	Aptian limestone	1.8	27.3
BJU5 cte2	Aptian limestone	1.6	26.7
6939U5	Aptian limestone	2.9	26.7
9518U5	Aptian limestone	3	27.3
6937A	Aptian limestone	3.5	27
B9514	Ankerite 1	2.7	26.8
9534B1	Ankerite 1	3.6	26.9
9534B2	Ankerite 1	3.1	26.9
9534A2	Ankerite 2	3	27
B9517A	Ankerite 2	2.5	26.3
B9517B	Ankerite 2	2.4	25.9
9575A	Ankerite 3	-0.4	19.6
9575B	Ankerite 3	0.3	21.2
B63W	Ankerite 3	1.5	22.9
BJ901 cte	Calcite 1	1.3	18.8
B8511G	Calcite 1	1.3	21.7
C18015*	Calcite 1	3.1	22.9
C18128*	Calcite 1	3.3	21.3
B92H	Calcite 1	3.8	23.1
B9530B	Calcite 2	3.1	24.8
B6911B	Calcite 2	3.1	26
9502	Calcite 2	2.6	25.6
9505	Calcite 2	3.7	25.9
6904A	Calcite 2	2.9	25.5
C18028*	Calcite 2	3.6	26.9
C1830*	Calcite 2	3.8	27.1
C18020*	Calcite 2	3.8	27.4
BJ2295	Calcite 2	6.2	26.4
9549B	Calcite 2	3.5	25.6
B6937B	Calcite 2	3.3	27.3

Table 4 Sulfur and oxygen isotopes compositions sphalerite, Galena, pyrite and barite from the different ore bodies collected from different ore zones at levels (–63. –69. and –95 m) of the Bou Jaber mine (gîte de l'Est), Epigenetic galena and pyrite disseminated in Aptian limestones; and sulfur and oxygen isotopes compositions of Triassic gypsum collected from different salt diapirs of the area. Analysis marked with asterisk are from Salmi-Louar 2004 and Salmi-Laouar et al. 2007). Calculated Temperatures are obtained using the equation $\delta ZnS-\delta PbS = (0.73/T^2).10^6$ (Ohmoto and Rye1979).

Ore zones	Level (m)	Samples	Mineral	δ^{34}(‰ (CDT)	δ^{18}O‰. (SMOW)	Δ Sph-Gn ‰	T°C
Sulfide-rich zone	-63	1/P4Ba	Barite	21.5	21.3		
Sulfide-rich zone	-63	2/89NGn	Gn	5.8		3.6	176
Sulfide-rich zone	-63	3/89NGn1	Gn	6.0		3.5	180
Sulfide-rich zone	-63	4/89NSP1	Sph	9.4			
Sulfide-rich zone	-63	5/89NSP1	Sph	9.5		3.7	168
Sulfide-rich zone	-63	6/89NBa1	Barite	22.6	21.7		
Sulfide-rich zone	-63	7/89V2Sp	Sph	9.5		4	152
Sulfide-rich zone	-63	8/89V1Sp	Sph	9.5			
Sulfide-rich zone	-63	9/89V1Gn	Gn	5.5			
Sulfide-rich zone	-63	10/89V1Ba	Barite	23.4			
Sulfide-rich zone	-63	11/89V2Sp	Sph	9.2			
Sulfide/barite zone	-63	12/90K1Gn	Gn	3.6			
Sulfide/barite zone	-63	13/90K2Gn	Gn	5.2			
Sulfide/barite zone	-63	14/90K3Gn	Gn	5.2			
Sulfide/barite zone	-63	15/90K1Ba	Barite	20.2			
Sulfide/barite zone	-63	16/90K2Ba	Barite	22.3			
Sulfide/barite zone	-63	17/90K3Ba	Barite	21.1	22.2		
Sulfide/barite zone	-63	18/90K4Ba	Barite	21.6			
Barite zone	-63	19/6316Gn	Gn	6.37			
Barite zone	-63	20/63W4Ba	Barite	22.7	21.3		
Barite zone	-63	21/90CGn	Gn	5.8			
Sulfide-rich zone	-69	22/90HGSp	Sph	9.2		3.2	200
Sulfide-rich zone	-69	23/90HGn	Gn	6.0			
Sulfide-rich zone	-69	24/41AGn1	Gn	7.1			
Sulfide-rich zone	-69	25/11AGn2	Gn	8.1			
Sulfide-rich zone	-69	26/8511Gn1	Gn	1.1			
Sulfide-rich zone	-69	27/8511Gn2	Gn	1.2			
Sulfide-rich zone	-69	28/8511Sp1	Sph	8.4			
Sulfide-rich zone	-69	29/8511Ba1	Barite	21.5	21.8		
Sulfide-rich zone	-69	30/15Ba	Barite	21.9			
Sulfide-rich zone	-69	31/16BGn	Gn	6.7			
Sulfide-rich zone	-69	32/69BGn1	Gn	7.1			
Sulfide-rich zone	-69	33/69BBa	Barite	23.2	23.3		
Sulfide-rich zone	-69	34/20Sp1	Sph	9.3		4.48	129
Sulfide-rich zone	-69	35/20Gn1	Gn	4.9			
Sulfide-rich zone	-69	36/20Sp2	Sph	8.6		3.77	165
Sulfide-rich zone	-69	37/20Gn2	Gn	4.8			
Sulfide-rich zone	-69	38/20Ba1	Barite	21.6			
Sulfide-rich zone	-69	39/20Ba2	Barite	22.3			
Sulfide-rich zone	-69	40/21DSp1	Sph	9.7			
Sulfide-rich zone	-69	41/21DGn	Gn	8.2			
Sulfide-rich zone	-69	42/21DBa11	Barite	22.8			
Sulfide-rich zone	-69	43/21DBa12	Barite	23.0			
Sulfide-rich zone	-69	44/25C3Gn	Gn	5.8			
Sulfide-rich zone	-69	45/25DGn1	Gn	4.7		4.7	119
Sulfide-rich zone	-69	46/25DSp2	Sph	9.5			
Sulfide-rich zone	-69	47/25DGn2l	Gn	5.6			
Sulfide-rich zone	-69	48/25DGn3	Gn	7.5			
Sulfide-rich zone	-69	49/25Sp1	Sph	9.4		3.5	181
Sulfide-rich zone	-69	50/25Sp2	Sph	9.3		3.4	187
Sulfide-rich zone	-69	51/25Sp3	Sph	9.9		4.0	154
Sulfide-rich zone	-69	52/25Gn1	Gn	5.9		3.5	181
Sulfide-rich zone	-69	53/25Gn2	Gn	5.9			
Sulfide-rich zone	-69	54/27Sp	Sph	9.4		3.8	164
Sulfide-rich zone	-69	55/27Gn	Gn	5.6			
Sulfide-rich zone	-69	56/48Ba1	Barite	22.0			
Sulfide-rich zone	-69	57/48Gn1	Gn	5.1			
Sulfide-rich zone	-69	58/69DSp1	Sph	8.9			
Sulfide/barite zone	-69	60/21DBa1	Barite	22.9	20.7		
Sulfide/barite zone	-69	61/21DGn2	Barite	23.4	22.5		
Sulfide/barite zone	-69	62/21G1Gn	Gn	5.3			

Sulfide/barite zone	-69	63/21G1Ba	Barite	24.5	
Sulfide/barite zone	-69	64/23GGn1	Gn	6.5	
Sulfide/barite zone	-69	65/23GBa1	Barite	23.0	
Sulfide/barite zone	-69	66/25BGn	Gn	4.9	
Sulfide/barite zone	-69	67/25BBa	Barite	22.3	
Sulfide/barite zone	-69	68/36Gn	Gn	6.0	
Sulfide/barite zone	-69	69/36Ba2	Barite	22.2	
Barite zone	-69	70/31Ba	Barite	22.5	
Barite zone	-69	71/32Ba1	Barite	22.5	
Barite zone	-69	72/32Gn	Gn	5.5	
Barite zone	-69	73/32Ba2	Barite	20.8	
Barite zone	-69	74/BJDBa	Barite	22.4	
Barite zone	-69	75/50Gn1	Gn	5.9	
Barite zone	-69	76/69Ba	Barite	22.6	
Barite zone	-69	77/60Ba	Barite	23.7	
Sulfide-rich zone	-95	78/5AGn1	Gn	5.4	
Sulfide-rich zone	-95	79/5AGn2	Gn	5.6	
Sulfide-rich zone	-95	805ABa	Barite	22.3	
Sulfide-rich zone	-95	81/5Aba	Barite	18.7	
Sulfide-rich zone	-95	82/514gn	Gn	7.6	
Sulfide-rich zone	-95	83/514B2	Barite	22.8	23.1
Sulfide-rich zone	-95	84/514AGn	Gn	5.6	
Sulfide-rich zone	-95	85/514ABa	Barite	21.2	21.8
Sulfide-rich zone	-95	87/17AGn	Gn	7.9	
Sulfide-rich zone	-95	88/17Aba	Barite	21.3	
Sulfide-rich zone	-95	89/34BaG1	Barite	21.3	
Sulfide-rich zone	-95	90/34BaG2	Barite	18.5	21.4
Sulfide/barite zone	-95	91/34BaG2	Barite	18.6	
Sulfide/barite zone	-95	92/33BaG2	Barite	22.8	
Sulfide/barite zone	-95	93/33BaG3	Barite	20.7	
Barite zone	-95	94/33BaG3	Barite	20.8	
Barite zone	-95	95/98K3Sp	Sph	9.7	
Barite zone	-95	96/98K3Gn	Gn	7.0	
Barite zone	-95	97/98K3Ba	Barite	20.8	
Barite zone	-95	98/98Ba	Barite	19.9	
Barite zone	-95	99/95K3Ba	Barite	23.4	23.4
Barite zone	-95	100/C31Ba	Barite	21.3	
Barite zone	-95	101/60 int	Barite	23.0	21.8
Barite zone	-95	102/60 ext	Barite	22.0	19.6
Aptian limestone	Open pit	103*	Pyrite	15.6	
Aptian limestone	Open pit	104*	Pyrite	15.2	
Aptian limestone	Open pit	105*	Pyrite	16.2	
Aptian limestone	Open pit	106BJ1*	Gn	5.7	
Aptian limestone	Open pit	107CN*	Gn	7.2	
Aptian limestone	Open pit	108BJ2*	Gn	7.2	
Aptian limestone	Open pit	109N6*	Gn	9.6	
Aptian limestone	Open pit	110N2*	Gn	3.2	
Triassic sulfate	Ouenza	112 SA870*	Gypsum	16.0	
Triassic sulfate	Ouenza	113SA8729*	Gypsum	13.4	
Triassic sulfate	Ouenza	114SA8731*	Gypsum	14.3	
Triassic sulfate	Mesloula	115SA7982*	Gypsum	15.4	
Triassic sulfate	Mesloula	116SA8734*	Gypsum	15.2	
Triassic sulfate	Mesloula	117SA8738*	Gypsum	14.9	
Triassic sulfate	Mesloula	118SA8737*	Gypsum	15.3	
Triassic sulfate	Mesloula	119SA873*	Gypsum	14.6	
Triassic sulfate	Mesloula	120SA8733*	Gypsum	15.1	
Triassic sulfate	Mesloula	121SA8739*	Gypsum	15.5	
Triassic sulfate	Mesloula	122SA8740*	Gypsum	14.9	
Triassic sulfate	Bou Jaber	123S10*	Gypsum	15.4	
Triassic sulfate	Bou Jaber	124S40*	Gypsum	14.6	
Triassic sulfate	Bou Jaber	125S26*	Gypsum	15.3	
Triassic sulfate	Bou Jaber	126S26*	Gypsum	13.4	
Triassic sulfate	Bou Jaber	127S40*	Gypsum	15.3	
Triassic sulfate	Bou Jaber	128SA8726*	Gypsum	15.1	
Triassic sulfate	Hameimat	129SA8722*	Gypsum	13.4	
Triassic sulfate	Hameimat	130SA8735*	Gypsum	14.8	
Triassic sulfate	Fedj el Adoum	131 FH	Gypsum	16.0	15.5
Triassic sulfate	Fedj el Adoum	132FH	Gypsum	17.1	12.9
Triassic sulfate	Fedj el Adoum	133FH	Gypsum	16.8	16.1

Table 5 Strontium isotope compositions of different barite generations from Bou Jaber (levels –69 m and –95 m) and of Triassic gypsum from the Bou Jaber Triassic salt diapir.

Ore stage	Sample	Mineral	$^{87}Sr/^{86}Sr$	Std dev.
Early barite	69BJP4	Barite	0.708210	0.000031
Second generation barite	6960	Barite	0.710811	0.000026
Second generation barite	6932	Barite	0.710117	0.000029
Second generation barite	6921	Barite	0.710179	0.000032
Second generation barite	9531	Barite	0.710000	0.000033
Second generation barite	9514I	Barite	0.710134	0.000017
Late stage barite	6960	Barite	0.710811	0.000026
Late stage barite	692G3	Barite	0.711408	0.000033
Late stage barite	6960G	Barite	0.711291	0.000031
Triassic sulfate	Triassic	Gypsum	0.708125	0.000044

Table 6 Lead isotope composition of galena samples from Bou Jaber collected mine levels –69m and –95m)

Samples	$^{206}Pb/^{204}Pb$	$^{207}Pb/^{204}Pb$	$^{208}Pb/^{204}Pb$
6911AGn1	18.737	15.643	38.767
6911AGn2	18.707	15.671	38.808
6921DGn	18.730	15.678	38.838
6925C3Gn	18.704	15.643	38.779
6925BGn1	18.699	15.649	38.751
6932Gn1	18.732	15.690	38.869
6936Gn1	18.707	15.670	38.806
6948Gn	18.719	15.668	38.797
6950Gn1	18.720	15.673	38.797
955ABGn1	18.783	15.762	39.100
698511G	18.733	15.664	38.816
955BGn1	18.786	15.757	39.085
9514AGn	18.755	15.664	38.821
9514BGn	18.699	15.646	38.736
9517Gn	18.729	15.686	38.838
9598K3	18.752	15.663	38.805